Supplementary Information

Superhydrophobic Fluorinated Metal-organic Framework (MOF) Devices for High-efficiency Oil-water Separation

Jiaqi Ma,[‡a] Mingshi Zhang,[‡a,b] Rui Feng,[c] Lu Dong,[a] Wei Sun,[d] and Yanyuan Jia[*a,e]

[a]College of Chemistry and Chemical Engineering, Inner Mongolia University, Hohhot 010021, P. R. China

[b]Department of Chemistry and Biochemistry, University of California, San Diego, La Jolla, California 92093, United States

[c]School of Materials Science and Engineering, Smart Sensing Interdisciplinary Science Center, Nankai University & TKL of Metal and Molecule Based Material Chemistry, Tianjin 300350, P. R. China

[d]Department of Chemistry, University of Michigan, Ann Arbor, MI 48109, United States

[e]Key Laboratory of Advanced Energy Materials Chemistry (Ministry of Education), Nankai University, Tianjin 300071, P. R. China

Contents

S1. Synthesis of ligands

S1.1. Synthesis of 2-fluoroterephthalic acid.[1]

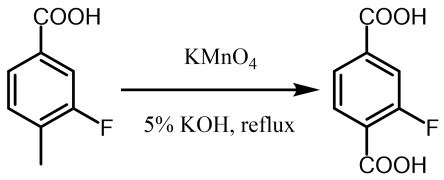

Scheme S1. Synthesis of 2-fluoroterephthalic acid

3-fluoro-4-methylbenzoic acid (900 mg, 5.85 mmol) and $KMnO_4$ (3.09 g, 19.26 mmol) were dissolved in 5% KOH aqueous solution (30 mL) and the mixture was refluxed for 6 hours. The solution was then cooled to room temperature and stirred for another day. After filtration, concentrated HCl solution (~ 37%) was added to the filtrate until the pH reached around 1. The white precipitate was collected by filtration and then washed with water (20 mL). The obtained solid was dried under vacuum to afford 2-fluoroterephthalic acid as a white powder (812 mg, 75.4 %).

^{1}H NMR (500 MHz, DMSO-*d*$_6$) δ 13.58 (s, 2H), 7.98 – 7.95 (m, 1H), 7.83 (dd, *J* = 8.1, 1.6 Hz, 1H), 7.73 (dd, *J* = 11.0, 1.6 Hz, 1H); **^{19}F NMR (470 MHz, DMSO-*d*$_6$)** δ -110.18 – -110.28 (m, 1F).

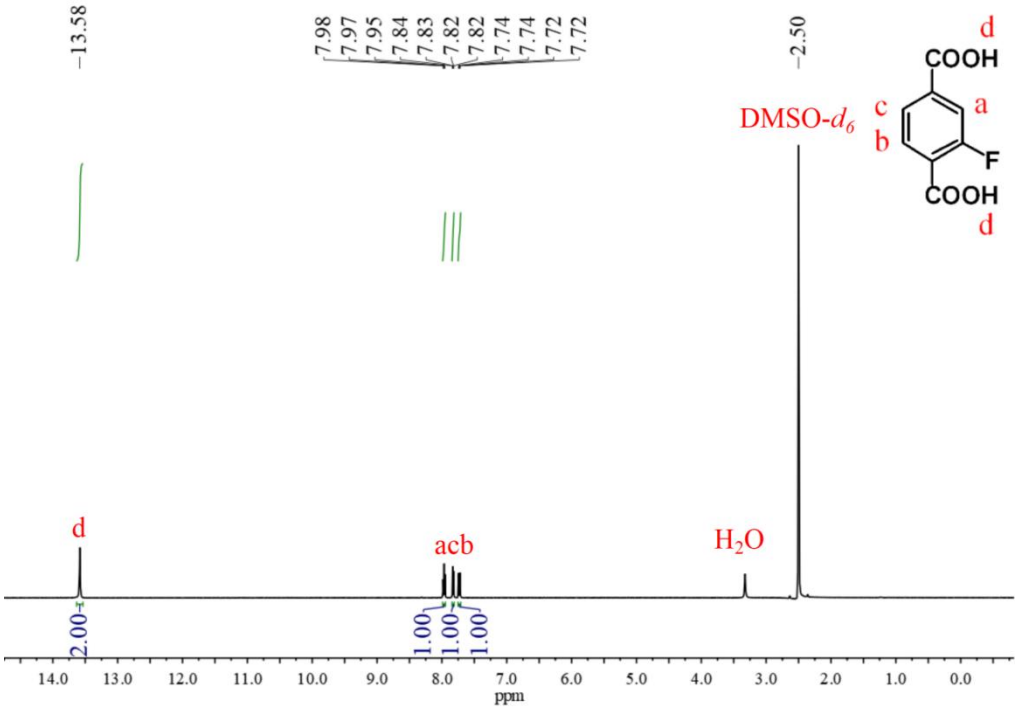

Figure S1. ^{1}H NMR spectrum of 2-fluoroterephthalic acid in DMSO-*d*$_6$ (500 MHz) recorded at 298 K.

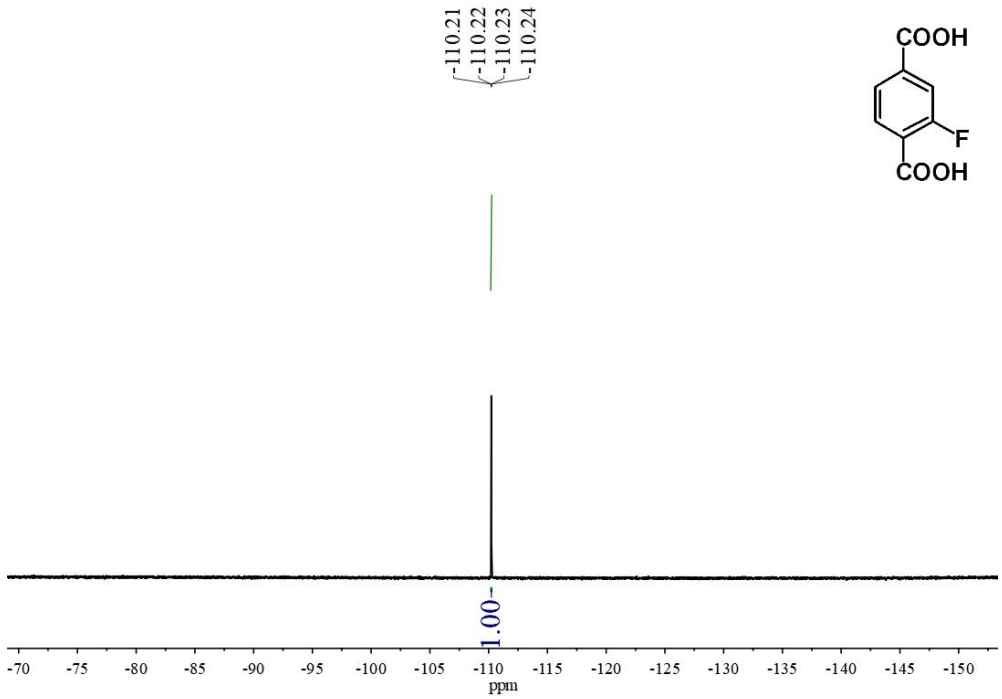

Figure S2. ^{19}F NMR spectrum of 2-fluoroterephthalic acid in DMSO-d_6 (470 MHz) recorded at 298 K.

S1.2. Synthesis of 2,5-difluoroterephthalic acid.[2]

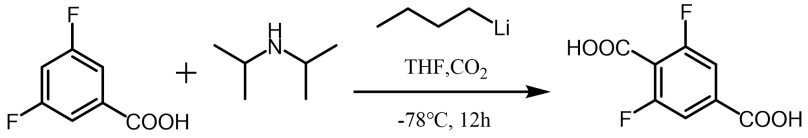

Scheme S2. Synthesis of 2,5-difluoroterephthalic acid

Dry tetrahydrofuran (20 mL), anhydrous diisopropylamine (1.74 mL, 12.4 mmol), and n-butyllithium (5.1 mL, 12.7 mmol, 2.5 M in hexane) were added to a round bottom flask under a nitrogen atmosphere at -78 °C. The mixture was allowed to react for 1 hour with stirring. 3,5-difluorobenzoic acid (948.6 mg, 6 mmol) was dissolved in 10 mL of dried tetrahydrofuran and added into the mixture dropwise for 2 hours. Crushed dry ice (10 g) was added to the reaction. Then, the reaction was allowed to warm to room temperature within 4 hours. At the end of the reaction, the reaction was cooled down to room temperature, and the concentrated HCl solution (~ 37%) was acidified to pH = 1 and extracted with anhydrous diethyl ether three times. The organic layer was collected and washed three times with deionized water and saturated sodium chloride solution, dried with anhydrous magnesium sulfate, and filtered. The diethyl ether solvent was removed using a rotary evaporator, and the solid product was collected. The product was further purified by recrystallization in a mixture of hexane-acetone. Pure 2,5-difluoroterephthalic acid (0.69 mg) was isolated as a light yellow powder in 56.5% yield.

^{1}H NMR (600 MHz, DMSO-d_6) δ 13.88 (s, 2H), 7.64 – 7.63 (m, 2H); **^{19}F NMR (565 MHz, DMSO-d_6)** δ -111.15 (d, J = 7.6 Hz, 2F).

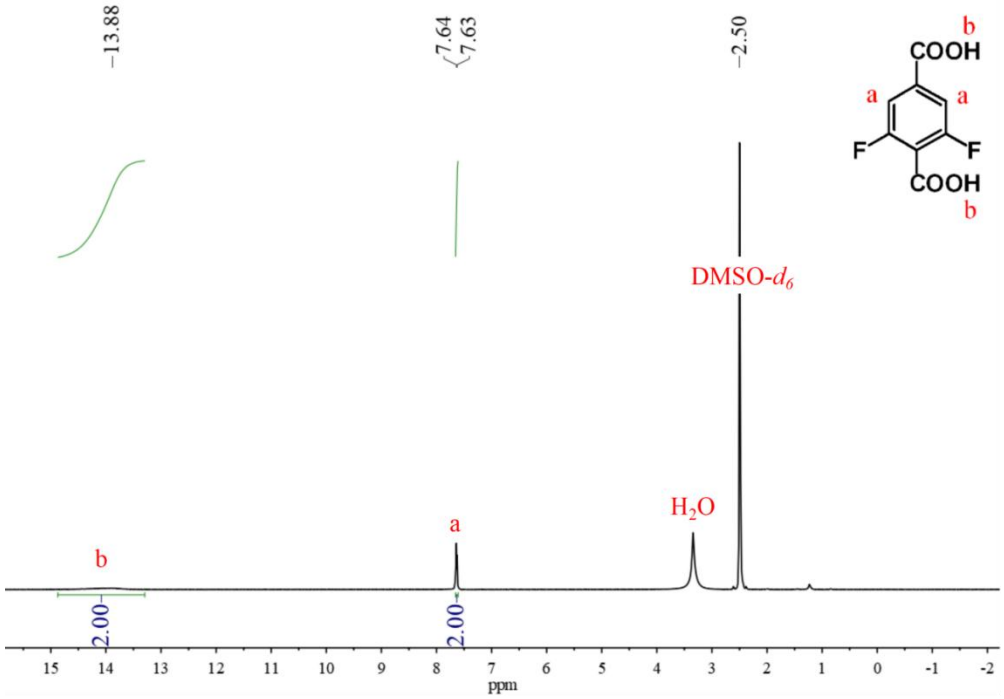

Figure S3. ^{1}H NMR spectrum of 2,5-difluoroterephthalic acid in DMSO-d_6 (600 MHz) recorded at 298 K.

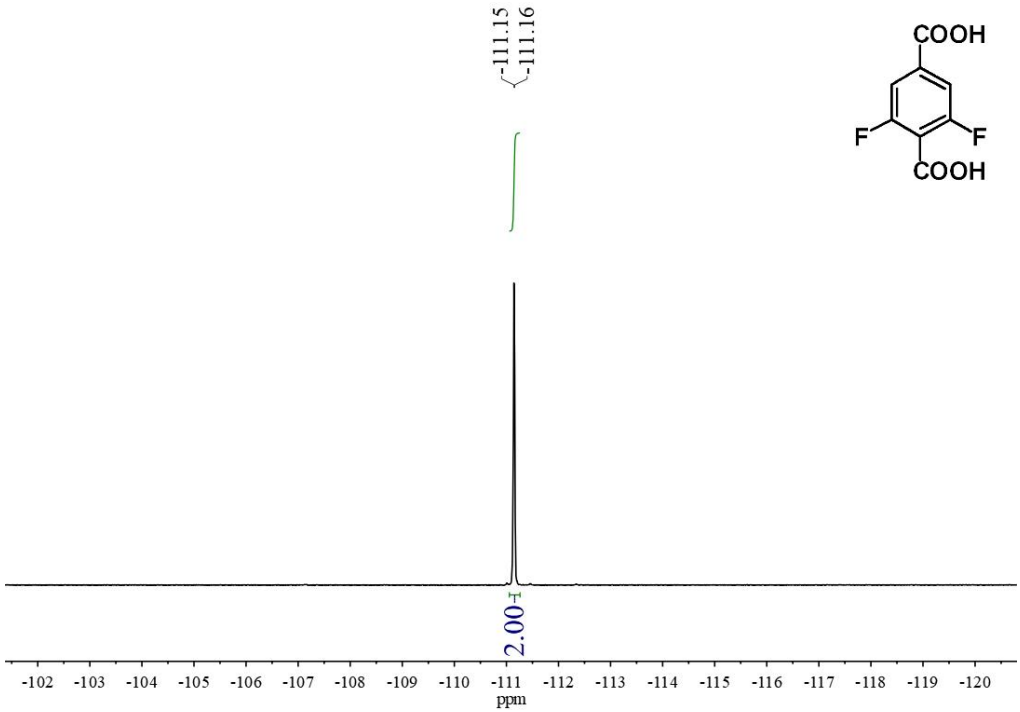

Figure S4. ^{19}F NMR spectrum of 2,5-difluoroterephthalic acid in DMSO-d_6 (565 MHz) recorded at 298 K.

S1.3. Synthesis of 2-(trifluoromethyl) terephthalic acid.[3]

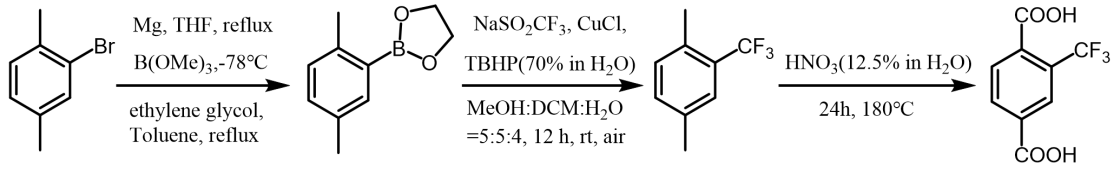

Scheme S3. Synthesis of 2-(trifluoromethyl)terephthalic acid.

Synthesis of 2-(2,5-dimethylphenyl)-1,3,2-dioxaborolane. Freshly ground magnesium strips (1.07 g, 44 mmol) were added to dry tetrahydrofuran (55 mL). A part of the solution of 2,5-dimethyl bromobenzene (5.52 mL, 40 mmol) was added to the solution dropwise under a nitrogen atmosphere. Hot air is used to initiate the reaction until the solution changes from yellow to colorless, and the remaining 2,5-dimethyl bromobenzene is added. The mixture was heated to 76 °C and refluxed for 1.5 hours, and then the solution was cooled down to room temperature. Trimethyl borate was dissolved in dry THF (55 mL, 1.45 mM) and then added to the mixture dropwise at -78 °C. Then, the greyish solution was warmed up to room temperature and concentrated to dryness by reduced-pressure rotary evaporation. Ethanol glycol (18 mL) and toluene (55 mL) were added to the resulting solid. The mixture was refluxed overnight at 95 °C, and the toluene layer was separated and concentrated by a reduced-pressure rotary evaporator. The turbid liquid was further dried by vacuum distillation to obtain the final product (6.99 g, yield: 88%).

^{1}H NMR (600 MHz, $CDCl_3$) δ 7.63 (s, 1H), 7.17 (d, J = 5.5 Hz, 1H), 7.08 (d, J = 7.7 Hz, 1H), 4.37 (s, 4H), 2.50 (s, 3H), 2.31 (s, 3H).

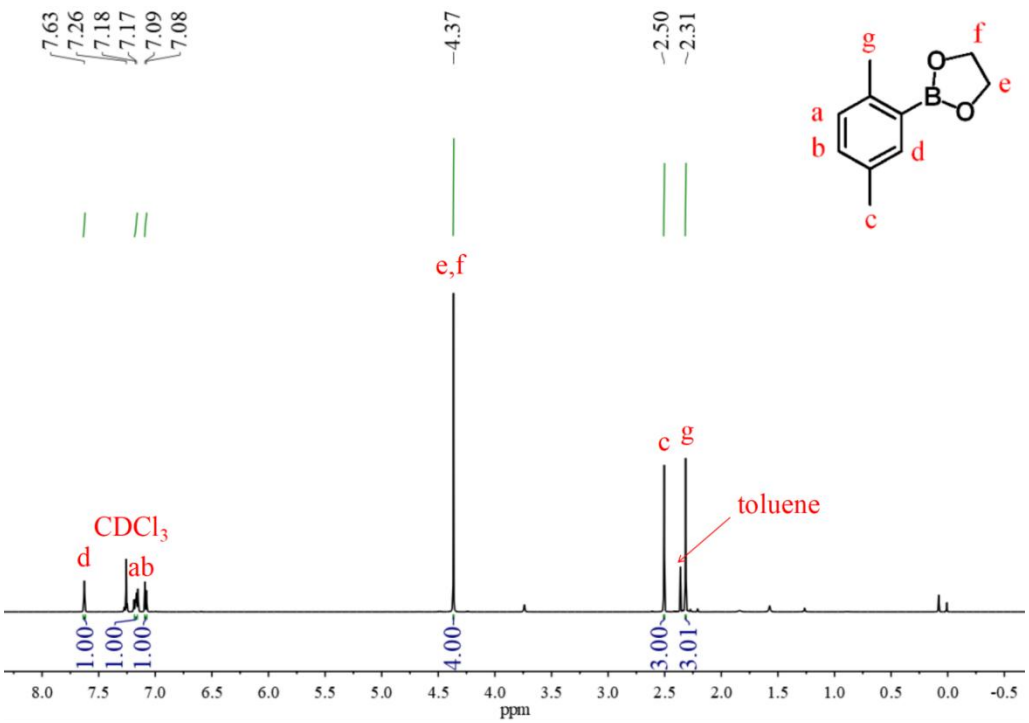

Figure S5. ^{1}H NMR spectrum of 2-(2,5-dimethylphenyl)-1,3,2-dioxaborolane in $CDCl_3$ (600 MHz) recorded at 298 K.

Synthesis of 1,4-dimethyl-2-trifluoromethyl-benzene. Under 0 °C, CuCl (2.97 g, 30 mmol), $NaSO_2CF_3$ (14.05 g, 90 mmol), and 2-(2,5-dimethylphenyl)-1,3,2-dioxaborolane (5.28 mg, 30 mmol) was added to a mixture of DCM/MeOH/H_2O (50 mL/50 mL/40 mL) in a round bottom flask. Tert-butyl hydroperoxide (TBHP, 70% w/w in water, 18 mL, 150 mmol) was added dropwise. The reaction was allowed to warm to room temperature and stirred for 12 h. At the end of the reaction, anhydrous diethyl ether was added and extracted three times. The organic layer was washed three times with saturated sodium bicarbonate solution and saturated sodium sulfite solution, respectively. The organic layer was dried with anhydrous magnesium sulfate. The filtrate was concentrated by a rotary evaporator without further purification.

^{1}H NMR (600 MHz, $CDCl_3$) δ 7.41 (s, 1H), 7.21 (d, *J* = 7.7 Hz, 1H), 7.15 (d, *J* = 7.7 Hz, 1H), 2.43 (s, 3H), 2.35 (s, 3H); **^{19}F NMR (565 MHz, $CDCl_3$)** δ -61.73 (s, 3F).

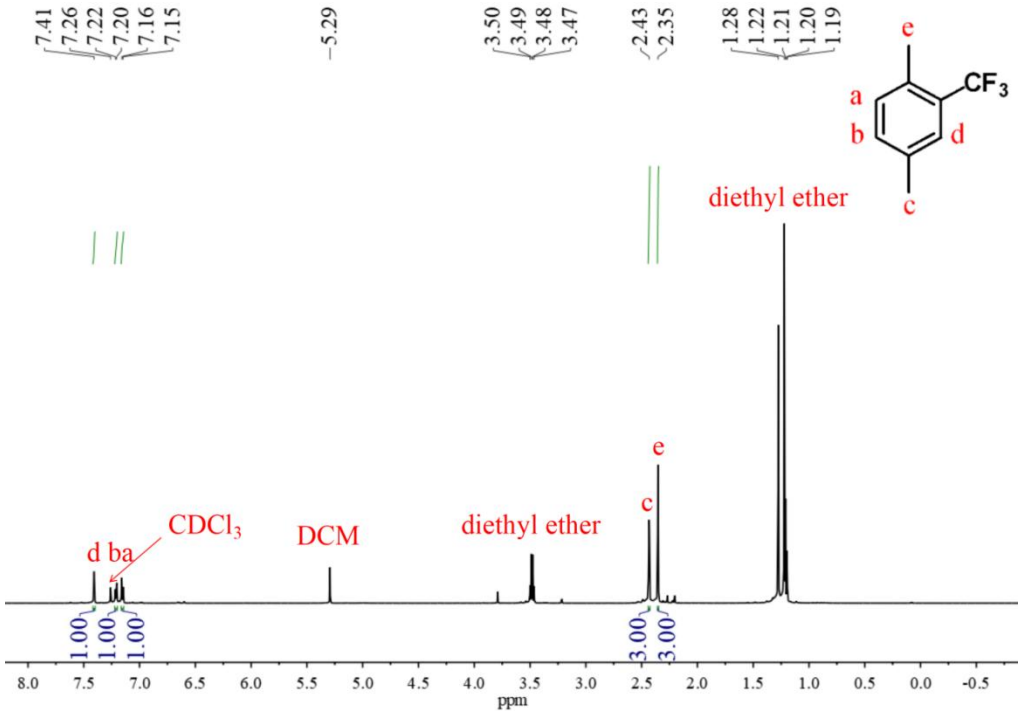

Figure S6. ^{1}H NMR spectrum of 1,4-dimethyl-2-trifluoromethyl-benzene in $CDCl_3$ (600 MHz) recorded at 298 K.

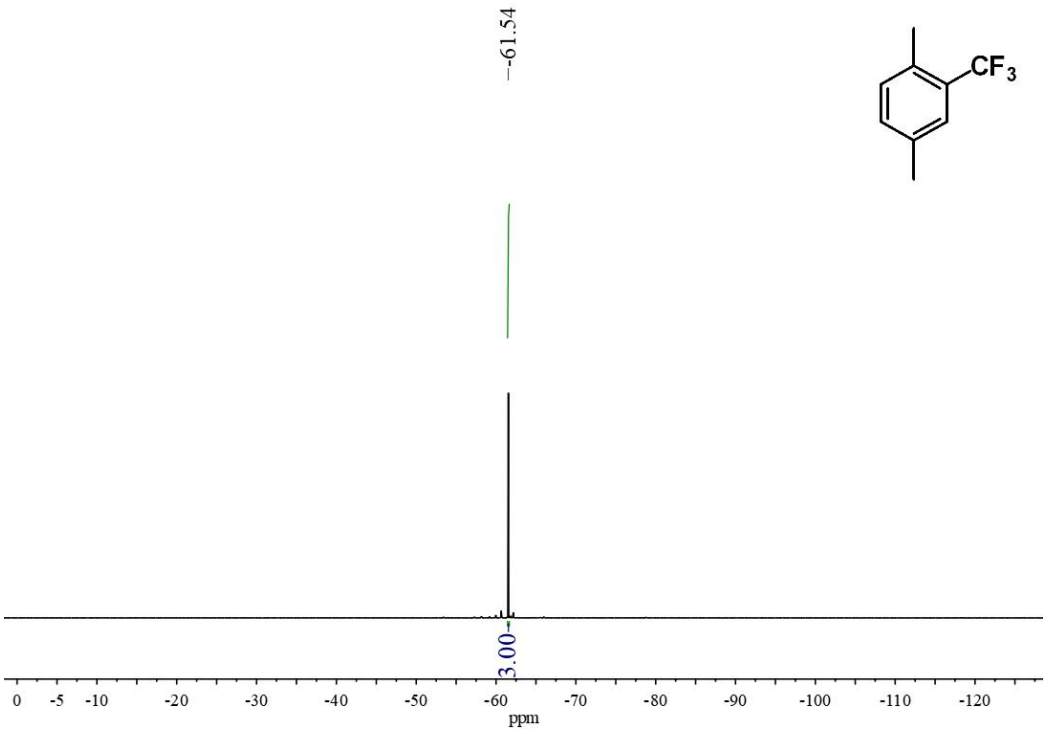

Figure S7. ^{19}F NMR spectrum of 1,4-dimethyl-2-trifluoromethyl-benzene in $CDCl_3$ (565 MHz) recorded at 298 K.

Synthesis of 2-(trifluoromethyl)terephthalic acid. 1,4-dimethyl-2-trifluoromethyl-benzene (870.8 mg, 5 mmol), water (4.8 mL), and nitric acid (12.5% in water, 9.7 mL) were added to a Teflon lined vessel (23 mL). The vessel was sealed and heated at 180 °C for 24 h. The resulting solid was collected by filtration and washed with water (10 mL) to afford a white solid product (108 mg, 72% yield).

^{1}H NMR (600 MHz, DMSO-*d*$_6$) δ 13.76 (s, 2H), 8.27 (d, *J* = 8.1 Hz, 2H), 7.94 (s, 1H); **^{19}F NMR (565 MHz, DMSO-*d*$_6$)** δ -58.48 (s, 3F).

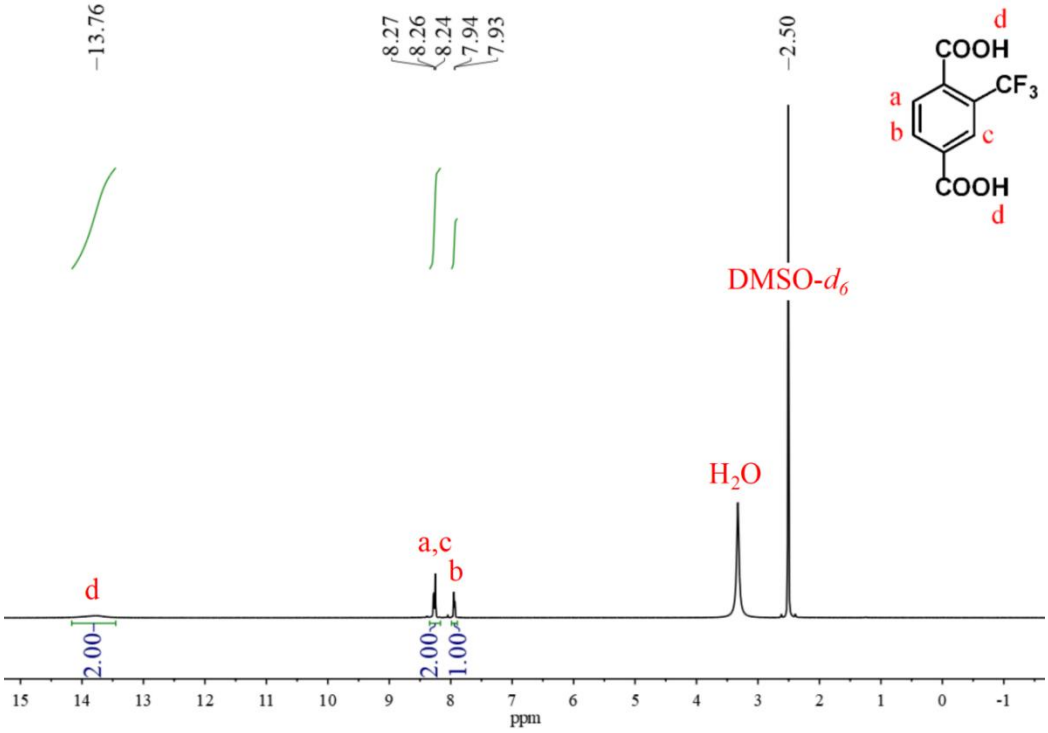

Figure S8. [1]H NMR spectrum of 2-(trifluoromethyl)terephthalic acid in DMSO-d_6 (600 MHz) recorded at 298 K.

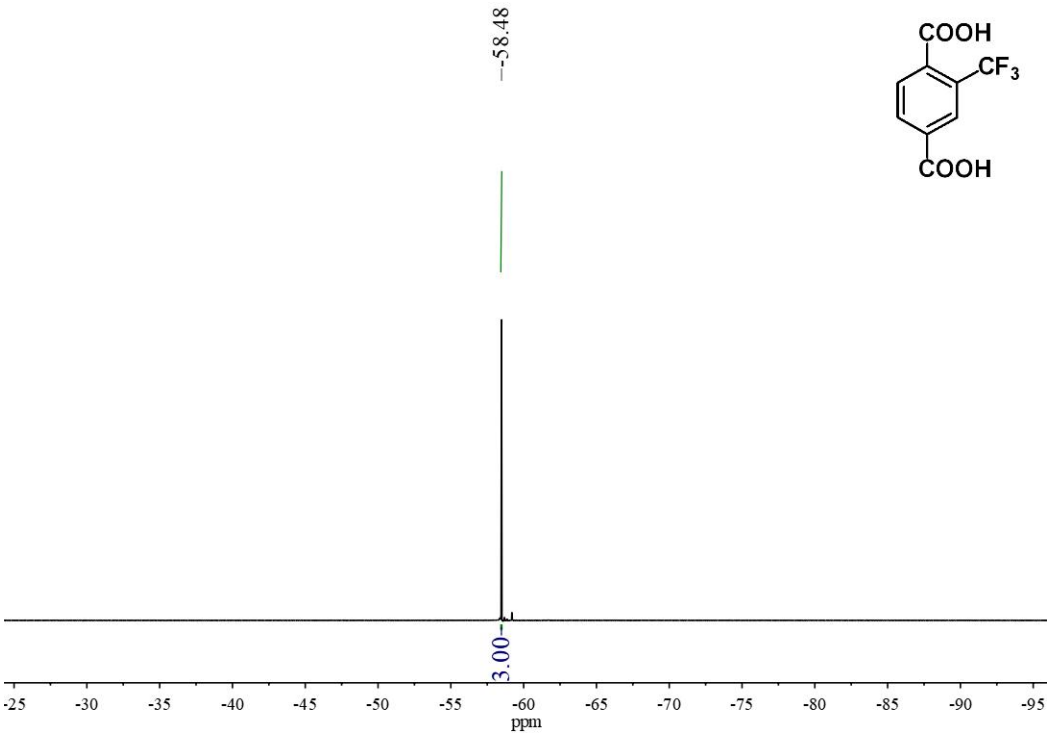

Figure S9. [19]F NMR spectrum of 2-(trifluoromethyl)terephthalic acid in DMSO-d_6 (600 MHz) recorded at 298 K.

S1.4. Synthesis of 2,5-ditrifluoromethylterephthalic acid.[4]

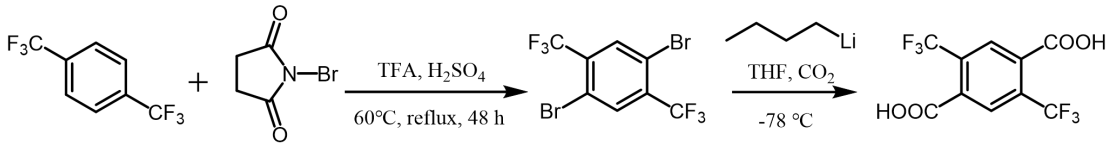

Scheme S4. Synthesis of 2,5-ditrifluoromethylterephthalic acid.

Synthesis of 2,5-dibromo-1,4-bis(trifluoromethyl)benzene. 1,4-bis(trifluoromethyl)benzene (2.14 g, 10 mmol), trifluoroacetic acid (SDS, 28 mL), and sulfuric acid (6.76 mL) were mixed and stirred under 60 °C for 10 min. Then, N-bromosuccinimide (3.5 g, 20 mmol) was slowly added over 30 min. The solution was heated to 60 °C under stirring for 48 h. After the addition of ice (100 g) to the crude mixture, the product was precipitated out. The solid product was separated by filtration and dried under vacuum for 24 hours. The product was purified by sublimation (under 75 °C) to obtain a white solid (1.78 g, 47.8% yield).

^{1}H NMR (600 MHz, $CDCl_3$) δ 8.01 (s, 2H); **^{19}F NMR (565 MHz, $CDCl_3$)** δ -63.57 (s, 6F).

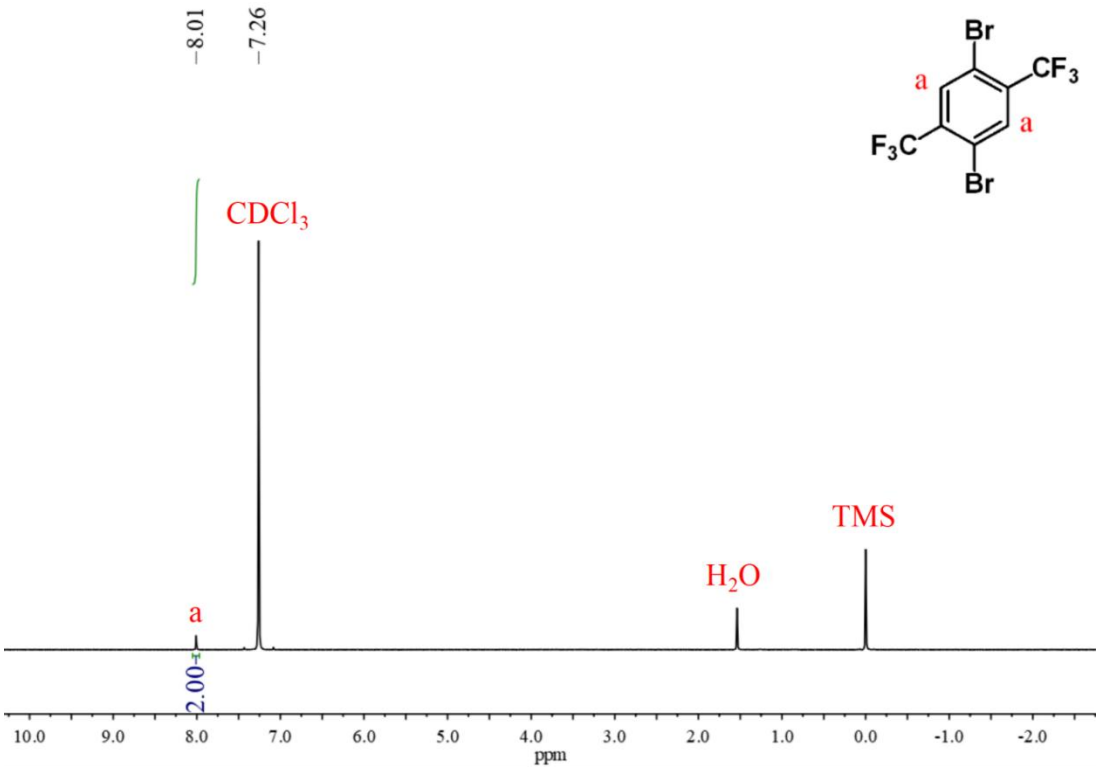

Figure S10. ^{1}H NMR spectrum of 2,5-dibromo-1,4-bis(trifluoromethyl)benzene in $CDCl_3$ (600 MHz) recorded at 298 K.

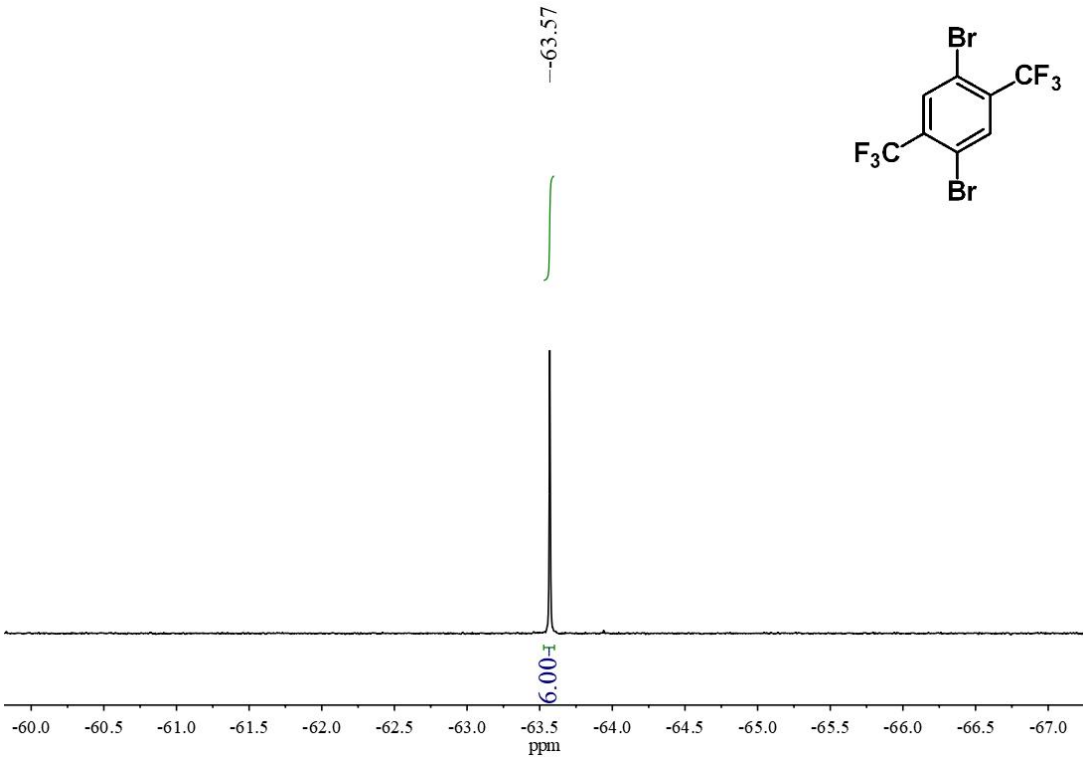

Figure S11. ^{19}F NMR spectrum of 2,5-dibromo-1,4-bis(trifluoromethyl)benzene in $CDCl_3$ (565 MHz) recorded at 298 K.

Synthesis of 2,5-ditrifluoromethylterephthalic acid. A solution of n-butyllithium (1.92 mL, 4.8 mmol, 2.5 M in hexane) was diluted with 3.75 mL of dry THF and cooled to -78 °C. Under a nitrogen atmosphere, 2,5-dibromo-1,4-bis(trifluoromethyl)benzene (0.8 g, 2.15 mmol) was dissolved in 5 mL of THF and added dropwise to the diluted n-butyllithium solution. After stirring for 30 minutes at -78 °C, 10 g of crushed dry ice was added to the mixture and the reaction was warmed up to room temperature. The mixture was extracted three times with 2 M sodium hydroxide solution. The aqueous phases were acidified by hydrochloric acid (12 M) to pH = 1. The precipitate was filtered and dried under vacuum for 24 h to give 0.5 g (73% yield) of 2,5-ditrifluoromethylterephthalic acid as a white solid.

^{1}H NMR (600 MHz, acetone-*d*$_6$) δ 8.30 (s, 2H); **^{19}F NMR (565 MHz, acetone-*d*$_6$)** δ -60.67 (s, 6F).

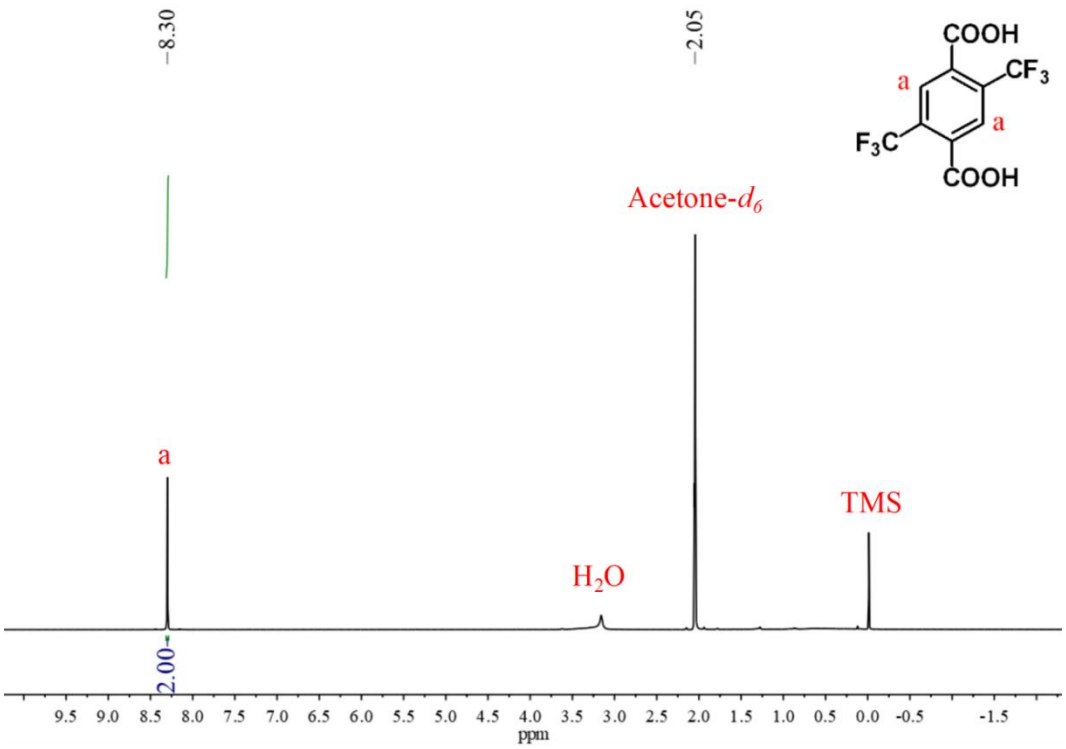

Figure S12. [1]H NMR spectrum of 2,5-ditrifluoromethylterephthalic acid in acetone-d_6 (600 MHz) recorded at 298 K.

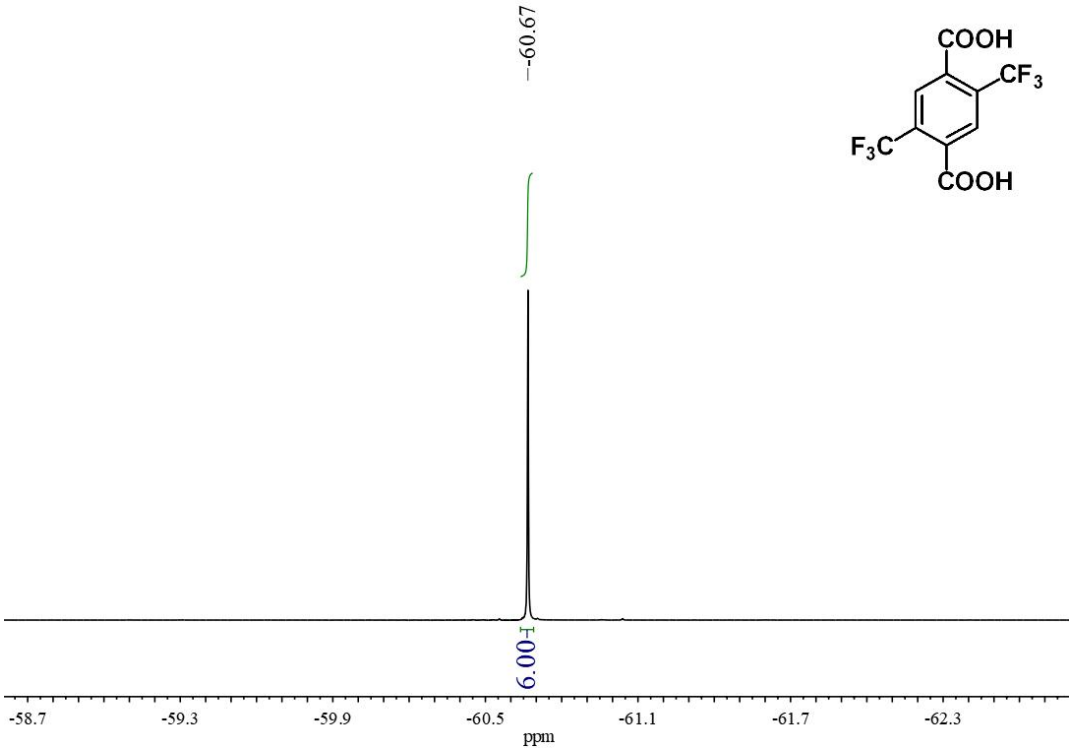

Figure S13. [1]H NMR spectrum of 2,5-ditrifluoromethylterephthalic acid in Acetone-d_6 (600 MHz) recorded at 298 K.

S2. Synthesis of fluorinated UiO-66

Synthesis of 1F-UiO-66. $ZrCl_4$ (0.0233 g, 0.1 mmol), 2-fluoroterephthalic acid (0.0184 g, 0.1 mmol), and benzoic acid (0.0122 g, 0.1 mmol) were fully dissolved in DMF (4 mL) in a kettle with polytetrafluoroethylene lining. The container was sealed and heated to 100 ℃ for 24 h in an oven. Then the temperature was gradually lowered to 25 ℃ over 6 hours. The white precipitate was collected by filtration and dried under the vacuum. The fluorinated UiO-66, 1F-UiO-66, is obtained with an 18% yield. FT-IR (KBr, cm^{-1}): 3430 (s), 1608 (s), 1512 (w), 1415 (m), 1365 (s), 1307 (m), 1267 (m), 1149 (s), 1064 (m), 925 (w), 796 (w), 659 (m), 605 (m).

Synthesis of 2F-UiO-66. A mixture of $ZrCl_4$ (0.0233 g, 0.1 mmol), 2,6-difluoroterephthalic acid (0.0202 g, 0.1 mmol), and benzoic acid (0.0122 g, 0.1 mmol) was completely dissolved in DMF (4 mL) in a kettle with polytetrafluoroethylene lining. The container was sealed and heated to 100 ℃ for 24 h in a baking oven. Then the temperature was progammablely lowered to 25 ℃ within 6 hours. The white precipitate was collected and dried under the vacuum. The target fluorinated UiO-66 is obtained with a yield of 17%, which is named 2F-UiO-66. FT-IR (KBr, cm^{-1}): 3413 (s), 2373 (w), 1652 (w), 1600 (s), 1500 (w), 1390 (s), 1297 (m), 1145 (s),1052 (m), 771 (m), 667 (m), 576 (w).

Synthesis of $1CF_3$-UiO-66. A mixture of $ZrCl_4$ (0.0233 g, 0.1 mmol), 2-(trifluoromethyl)-1,4-Benzenedicarboxylic acid (0.0234 g, 0.1 mmol), and benzoic acid (0.0122 g, 0.1 mmol) was completely dissolved in DMF (4 mL) in a kettle with polytetrafluoroethylene lining. The container was sealed and heated to 100 ℃ for 24 h in a baking oven. Then the temperature was progammablely lowered to 25 ℃ within 6 hours. The white precipitate was collected and dried under the vacuum. The target fluorinated UiO-66 is obtained with a yield of 18%, which is named $1CF_3$-UiO-66. FT-IR (KBr, cm^{-1}): 3434 (s), 1660 (s), 1602 (s), 1488 (m), 1407 (s), 1296 (w), 1253 (w), 1106 (s), 1035 (m), 891 (m), 788 (m), 659 (s), 594 (w).

Synthesis of $2CF_3$-UiO-66. A mixture of $ZrCl_4$ (0.0233 g, 0.1 mmol), 2,5-bis(trifluoromethyl)terephthalic acid (0.0302 g, 0.1 mmol), and benzoic acid (0.0122 g, 0.1 mmol) was completely dissolved in DMF (4 mL) in a kettle with polytetrafluoroethylene lining. The container was sealed and heated to 100 ℃ for 24 h in a baking oven. Then the temperature was progammablely lowered to 25 ℃ within 6 hours. The white precipitate was collected and dried under the vacuum. The target fluorinated UiO-66 is obtained with a yield of 18%, which is named $2CF_3$-UiO-66. FT-IR (KBr, cm^{-1}): 3413 (s), 1658 (s), 1589 (s), 1498 (m), 1417 (s), 1386 (s), 1228 (m), 1106 (s), 952 (w), 989 (w), 825 (w), 769 (m), 659 (s), 569 (m).

S3. Characterizations of fluorinated UiO-66

S3.1. SEM images.

Protocol: Fluorine-containing UiO-66 powder and stick it to the copper conductive adhesive on the sample holder. Gold was sprayed onto the sample before testing.

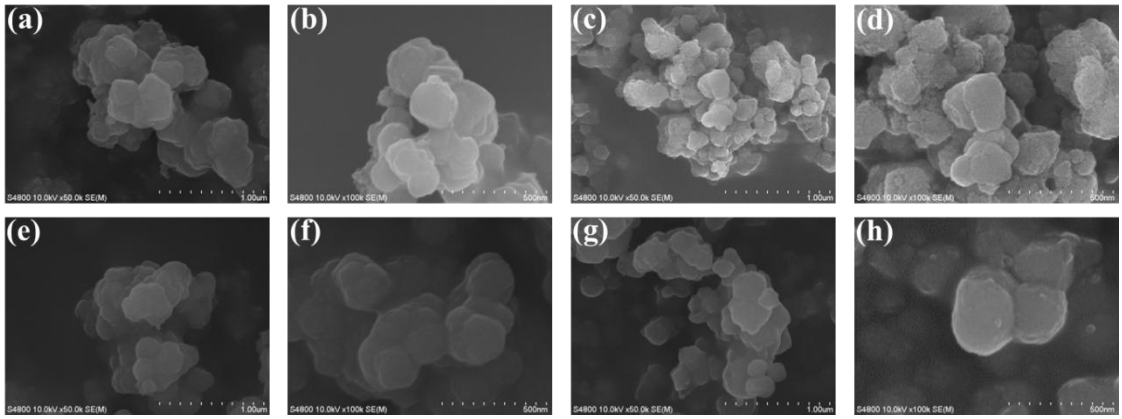

Figure S14. SEM images of (a, b). 1F-UiO-66; (c, d). 2F-UiO-66; (e, f). 1CF_3-UiO-66; (g, h). 2CF_3-UiO-66

S3.2. PXRD profiles

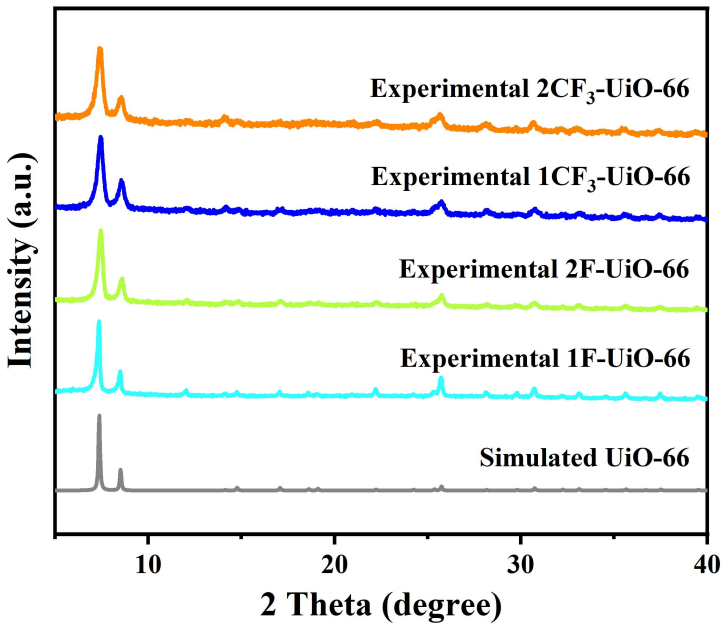

Figure S15. PXRD profiles of simulated UiO-66, synthesized 1F-UiO-66, 2F-UiO-66, 1CF_3-UiO-66, and 2CF_3-UiO-66.

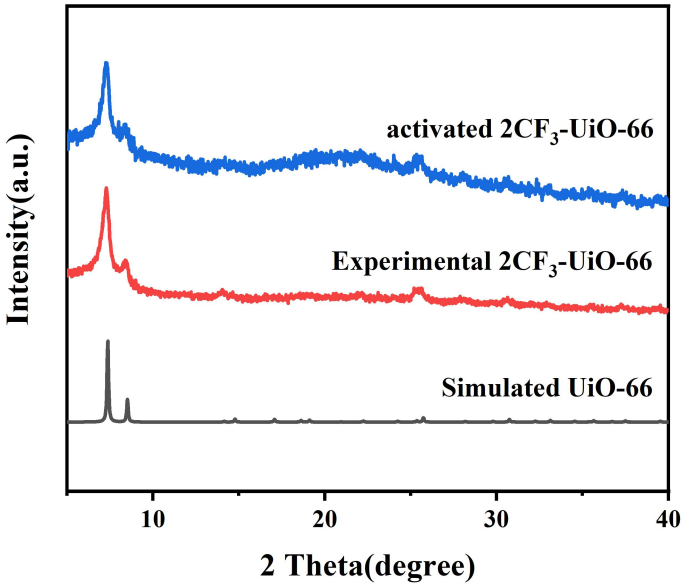

Figure S16. PXRD profiles of simulated UiO-66, experimental data of as-synthesized $2CF_3$-UiO-66, and activated $2CF_3$-UiO-66 under vacuum in a nitrogen atmosphere at 150 °C for 6 h.

S3.3. FT-IR spectra

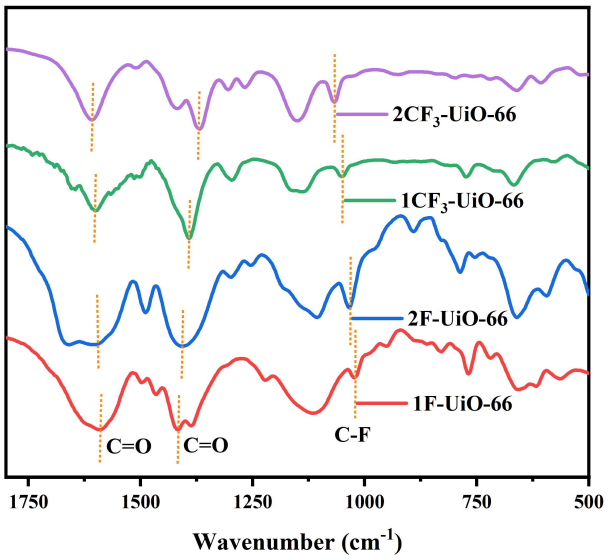

Figure S17. FT-IR spectra of 1F-UiO-66, 2F-UiO-66, $1CF_3$-UiO-66, and $2CF_3$-UiO-66.

S3.4. XPS characterization.

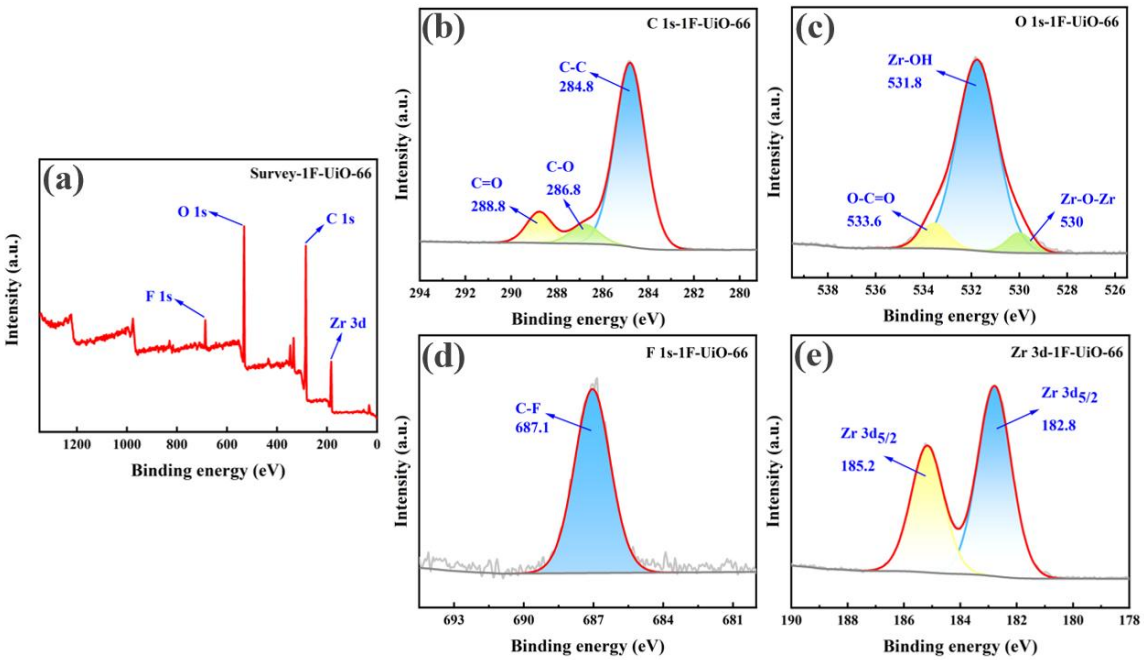

Figure S18. (a) A comparative XPS survey spectra of 1F-UiO-66, high-resolution XPS spectra of (b) C 1s, (c) O 1s, (d) F 1s, (e) Zr 3d of 1F-UiO-66.

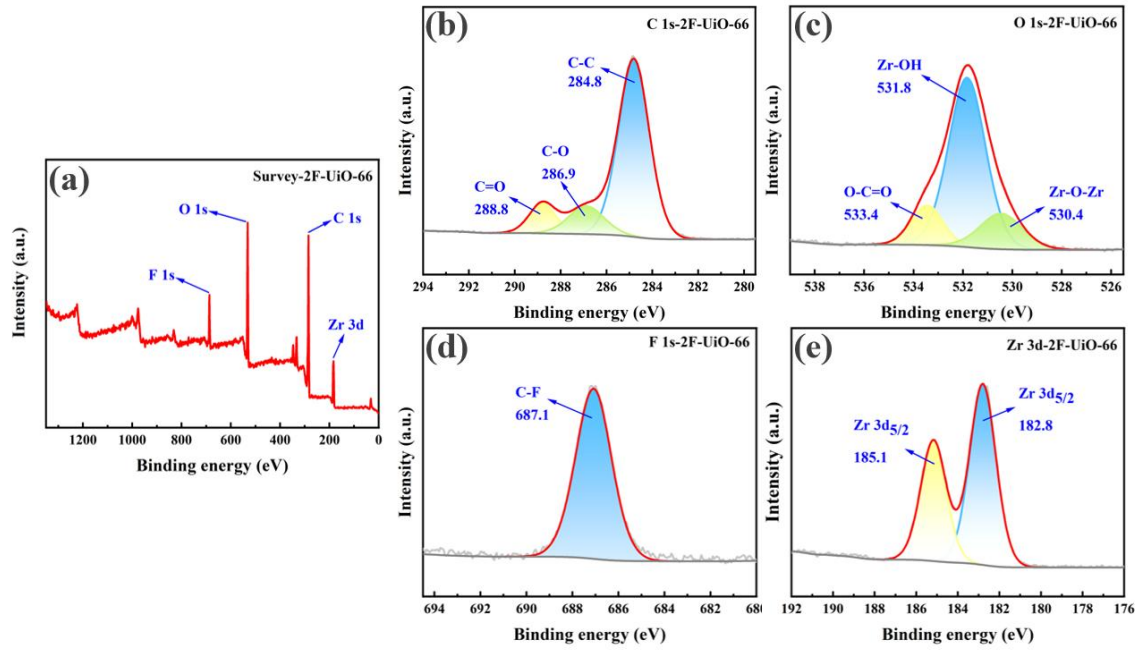

Figure S19. (a) A comparative XPS survey spectra of 2F-UiO-66, high-resolution XPS spectra of (b) C 1s, (c) O 1s, (d) F 1s, (e) Zr 3d of 2F-UiO-66.

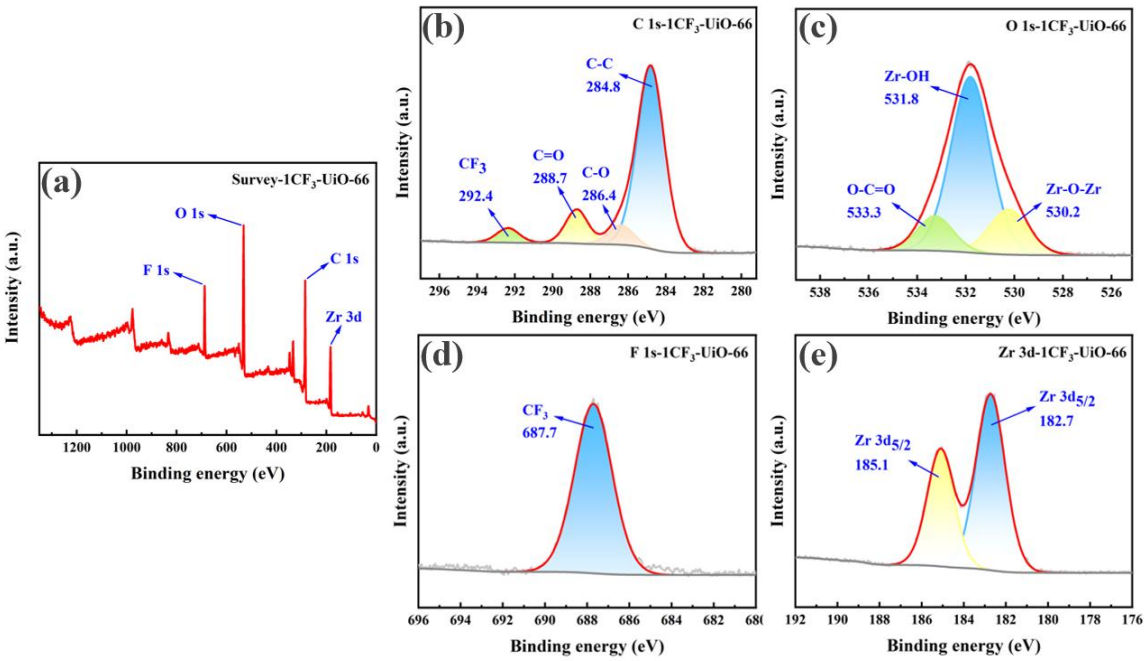

Figure S20. (a) A comparative XPS survey spectra of $1CF_3$-UiO-66, high-resolution XPS spectra of (b) C 1s, (c) O 1s, (d) F 1s, (e) Zr 3d of $1CF_3$-UiO-66.

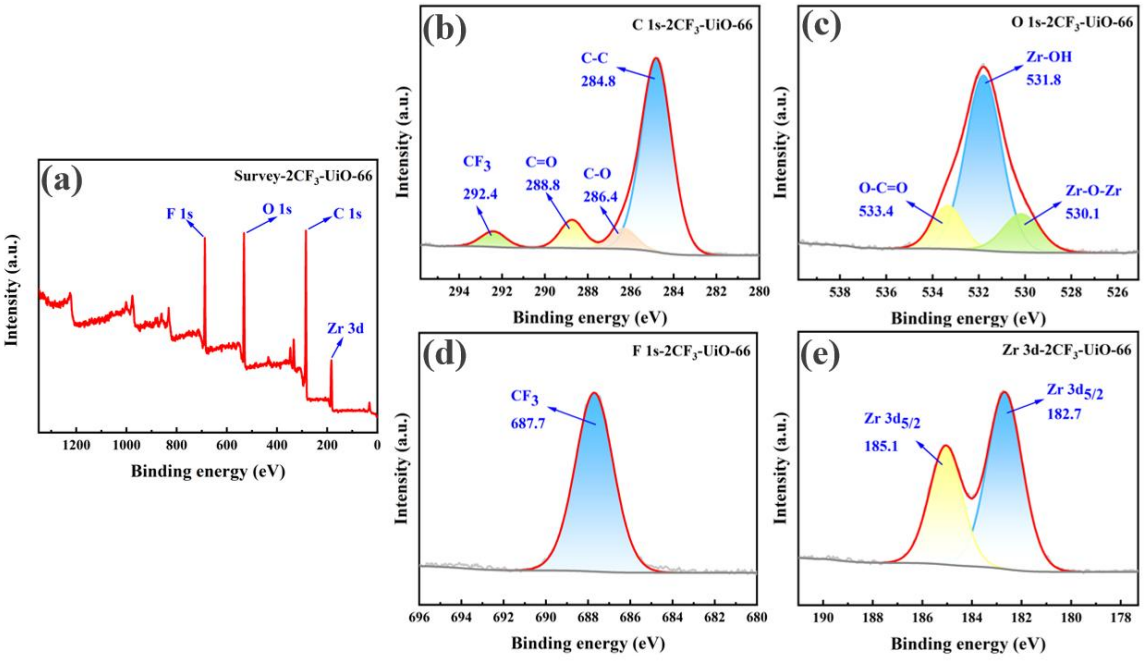

Figure S21. (a) A comparative XPS survey spectra of $2CF_3$-UiO-66, high-resolution XPS spectra of (b) C 1s, (c) O 1s, (d) F 1s, (e) Zr 3d of $2CF_3$-UiO-66.

S3.5. Hydrophobicity of fluorinated UiO-66 powders test.

The UiO-66, 1F-UiO-66, 2F-UiO-66, 1CF_3-UiO-66, and 2CF_3-UiO-66 powders (around 2 mg) were scattered on the surface of 6 mL deionized water, and all fluorinated MOF powders floated on the surface of the water, while UiO-66 powder would quickly settle on the bottom of the water.

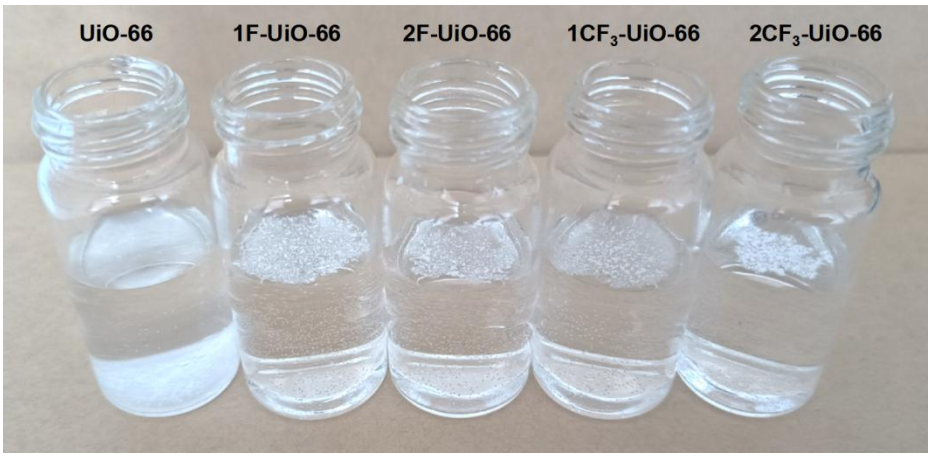

Figure S22. Images of 2 mg of adding UiO-66, 1F-UiO-66, 2F-UiO-66, 1CF_3-UiO-66, and 2CF_3-UiO-66 to 6 mL of DI water.

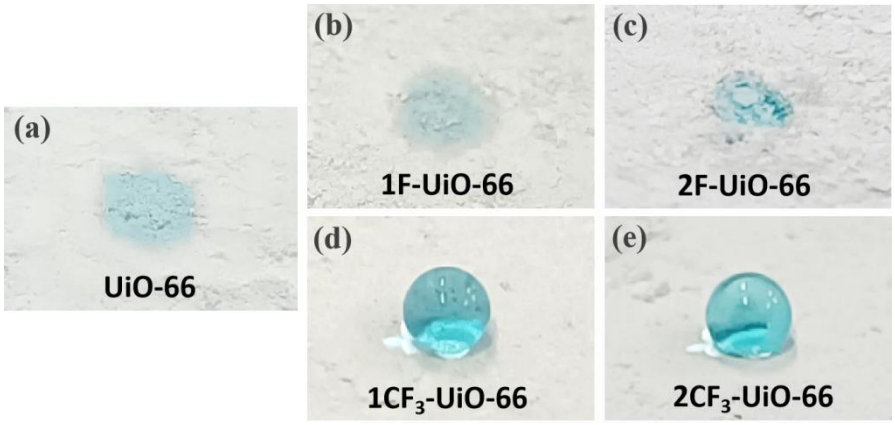

Figure S23. Images of water dripping on UiO-66, 1F-UiO-66, 2F-UiO-66, 1CF_3-UiO-66, and 2CF_3-UiO-66.

S3.6. Water contact angle.

Test method: the powder was fully compacted in the sample tank and tested with a water contact angle tester, and each drop fell about 5 μL.

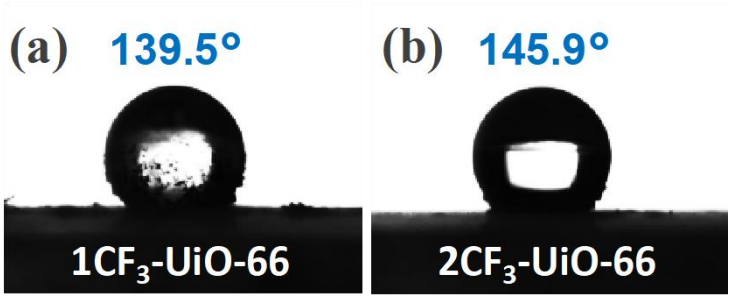

Figure S24. Images of water contact angle of (a) $1CF_3$-UiO-66 and (b) $2CF_3$-UiO-66 powders.

S3.7. Lipophilicity of $2CF_3$-UiO-66.

Test method: The $1CF_3$-UiO-66 and $2CF_3$-UiO-66 powder were put into the sample tank, and organic solvents dyed by Sudan I were dropped on the powder surface. The oil droplets were instantly absorbed.

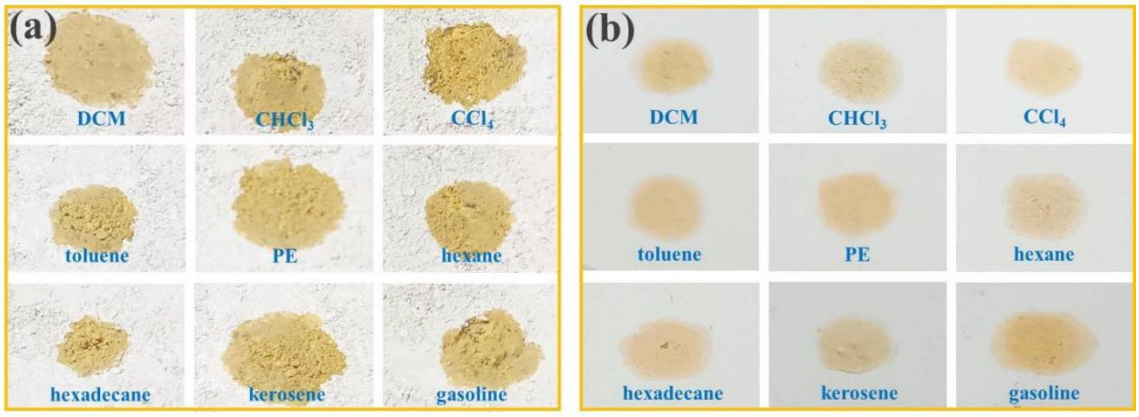

Figure S25. Images of adding different organic solvents to (a) $1CF_3$-UiO-66 and (b) $2CF_3$-UiO-66 powder.

S3.8. UV-vis absorption spectra of the selected synthesized MOFs

Protocol: 15 mg of 3,5-dichlorophenol was dissolved in 50 mL of deionized water. The mixture was sonicated for 2 hours as the mother solution. Then $1CF_3$-UiO-66 and $2CF_3$-UiO-66 of 10 mg were added to the 15 mL of mother solution and ultrasonicated for 2 hours. Then, the solutions were characterized by UV-vis spectra.

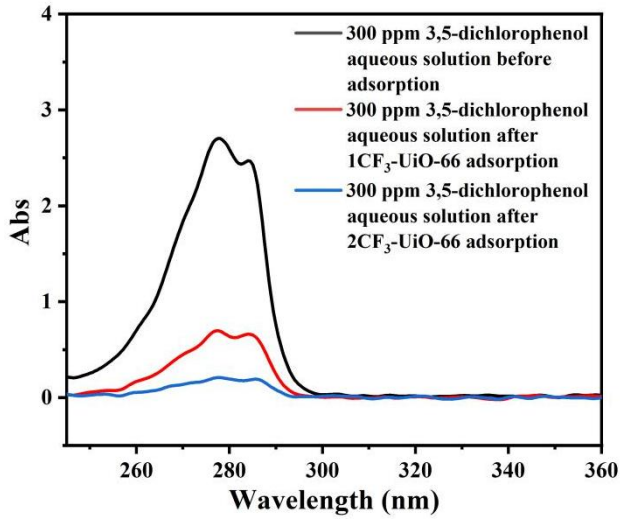

Figure S26. UV-vis spectra of 300 ppm 3,5-dichlorophenol aqueous solution before and after $1CF_3$-UiO-66 and $2CF_3$-UiO-66 adsorption.

S3.9. BET characterization

The activated $2CF_3$-UiO-66 powder was tested for N_2 adsorption and desorption at 77 K, and the specific surface area was 329 $m^2 \cdot g^{-1}$.

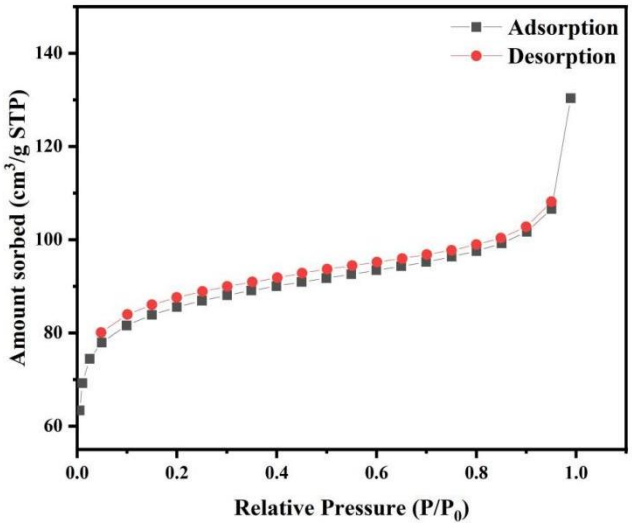

Figure S27. BET analysis of activated $2CF_3$-UiO-66.

S3.10. The water adsorption isotherms and oil components adsorption of fluorinated UiO-66.

Test method: UiO-66 and 2CF_3-UiO-66 powders were degassed at 160 °C for 5 h. These isotherms were measured at 25 °C

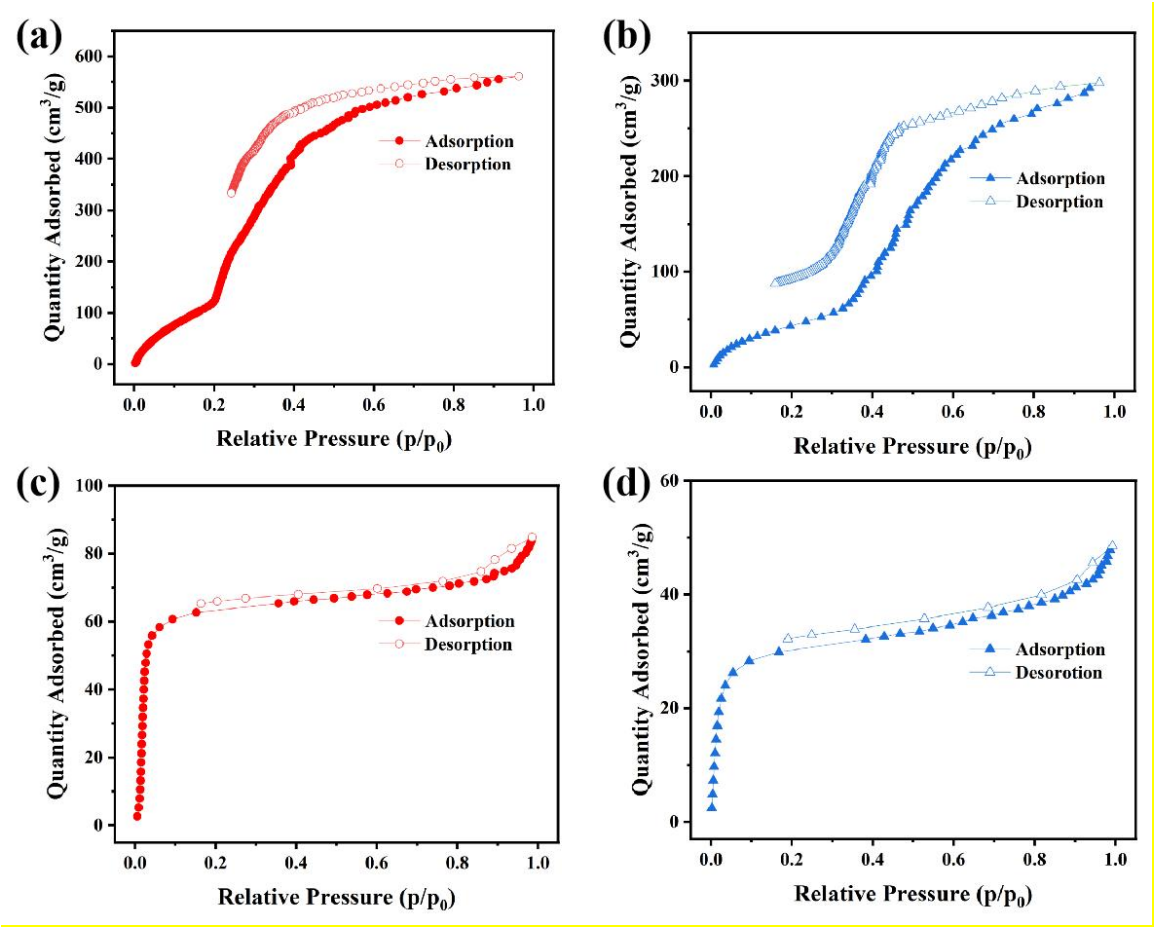

Figure S28. Water adsorption isotherms for (a) UiO-66 and (b) 2CF_3-UiO-66. Toluene adsorption isotherms for (c) UiO-66 and (d) 2CF_3-UiO-66.

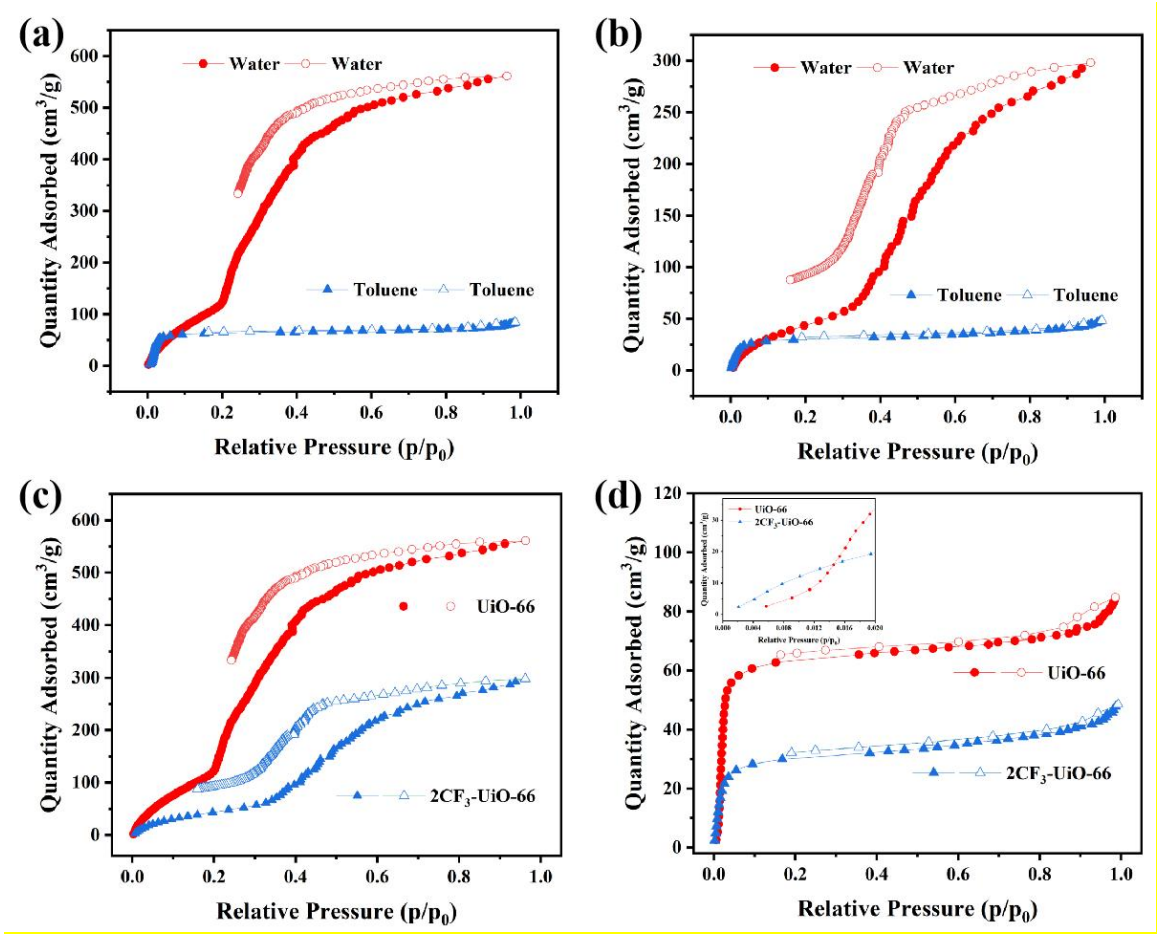

Figure S29. Water adsorption isotherms and toluene adsorption isotherms for (a) UiO-66 and (b) $2CF_3$-UiO-66. (c) Water adsorption isotherms and (d) toluene adsorption isotherms for UiO-66 and $2CF_3$-UiO-66.

S3.11. Solvent stability of $2CF_3$-UiO-66.

The $2CF_3$-UiO-66 powder material of 20 mg was soaked in 3 mL of different solvents for 24 hours, and the dried powder material was filtered and collected for PXRD characterization.

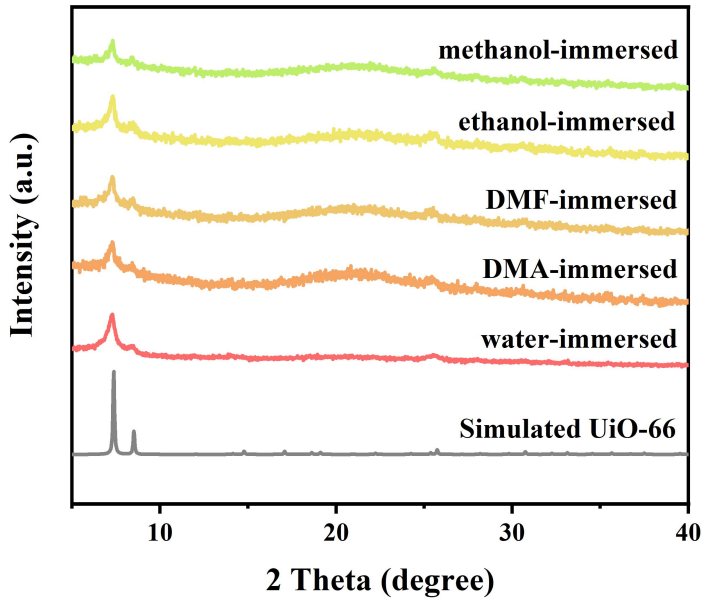

Figure S30. PXRD profiles of simulated UiO-66 and experimental data of $2CF_3$-UiO-66 after immersing in water, DMA, DMF, ethanol, and methanol for 24 h.

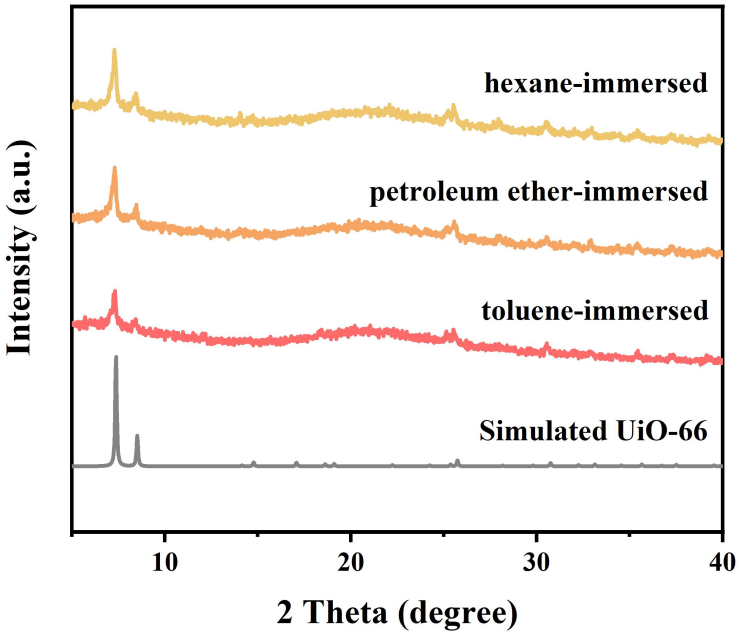

Figure S31. PXRD profiles of simulated UiO-66 and experimental data of $2CF_3$-UiO-66 after immersing in toluene, petroleum ether, and hexane for 24 h.

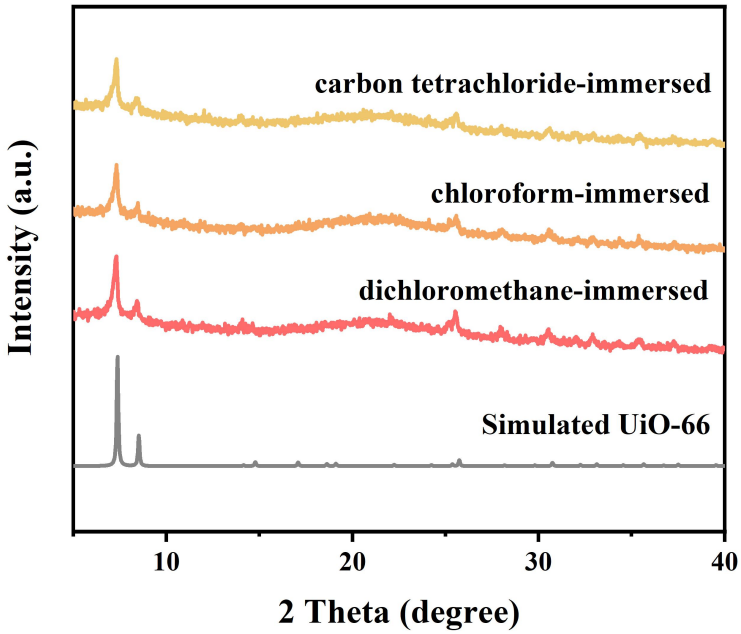

Figure S32. PXRD profiles of simulated UiO-66 and experimental data of $2CF_3$-UiO-66 after immersing in dichloromethane, chloroform, and carbon tetrachloride for 24 h.

S3.12. Acid-base stability of $2CF_3$-UiO-66.

The $2CF_3$-UiO-66 powder (20 mg) was soaked in 3 mL of an HCl/NaOH aqueous solution with pH=1-14 for 24 hours, and the powder was filtered and collected for the PXRD test.

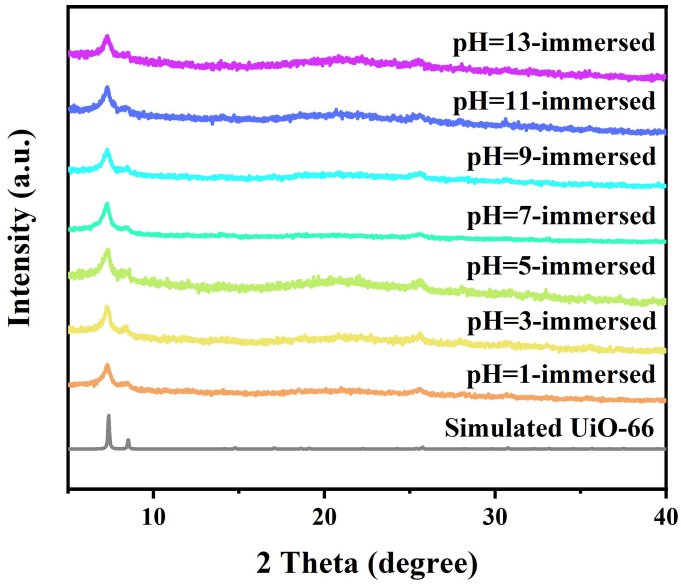

Figure S33. PXRD profiles of simulated UiO-66 and experimental data of $2CF_3$-UiO-66 after immersing in different pH aqueous solutions for 24 h.

S3.13. Thermogravimetric characterization

Activation of $2CF_3$-UiO-66: $2CF_3$-UiO-66 powder was suspended in ethanol under stirring. $2CF_3$-UiO-66 was filtered and re-suspended in fresh ethanol every 12 hours 3 times. The resulting $2CF_3$-UiO-66 was collected by filtration and activated under vacuum at 150 °C for 6 hours. The activated $2CF_3$-UiO-66 powder was tested by thermogravimetry.

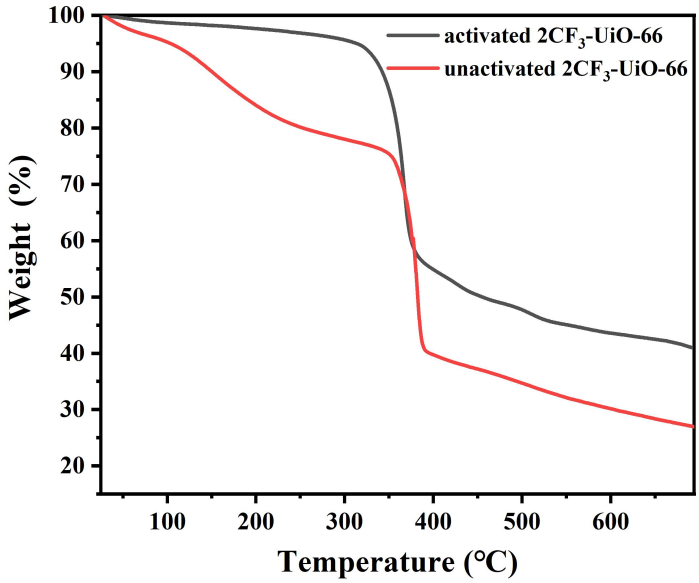

Figure S34. Thermogravimetric analysis of activated and unactivated $2CF_3$-UiO-66 (ramp rate: 5 °C/min) under an argon atmosphere.

S4. DFT calculation of fluorinated ligands

The liquid-water partition coefficients between n-octanol and water ($\log P_{\mathrm{oct/wat}}$) of the ligands were calculated using ORCA software package. During geometry optimization and frequency analysis procedure, PBE0 hybrid functional[5] with density functional theory (DFT)-D4 dispersion correction,[6] and def2-TZVP basis sets[7] were used together with the solvation model based on density (SMD) implicit solvation model[8]. The solvation free energy was calculated at M06-2X/6-31G* level,[9,10] and the high-level single point energy was calculated with PWPB95-D4[11] double-hybrid-meta-GGA density functionals and def2-TZVPP basis sets. The electrostatic isosurface map (isovalue=0.001) was processed using Multiwfn and drawn with visual molecular dynamics (VMD). The liquid-water partition coefficients were calculated according to the formula:

$$\log P_{\mathrm{oct/wat}} = -\frac{E_{\mathrm{octanol}} - E_{\mathrm{water}}}{2.303RT} \quad (1)$$

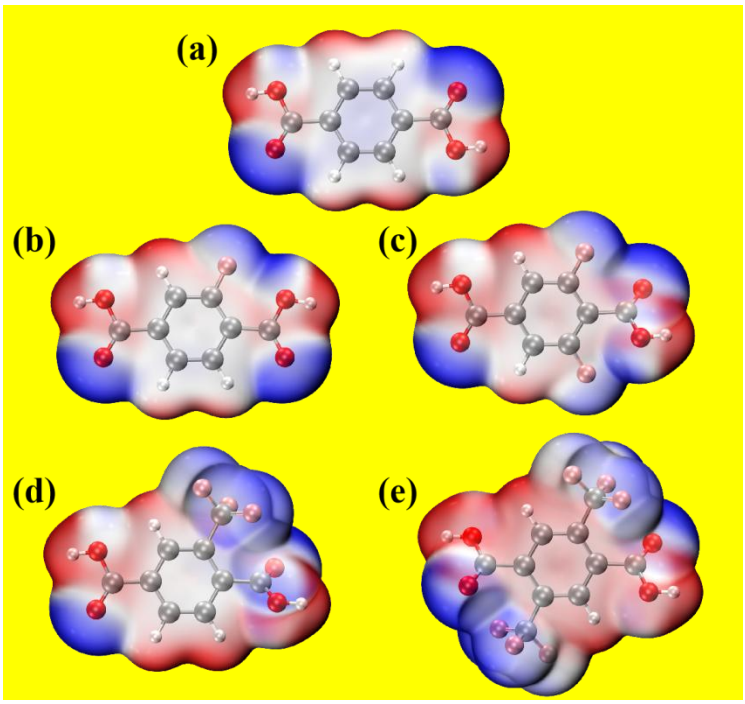

Figure S35. The optimized structure of (a) BDC (b) 1F-BDC (c) 2F-BDC (d) 1CF_3-BDC (e) 2CF_3-BDC.

Table S1. Energy and liquid-water partition coefficients of terephthalic acid and fluorinated terephthalic acid in water and n-octanol.

Ligands	BDC	1F-BDC	2F-BDC	1CF_3-BDC	2CF_3-BDC
			water		
E_1 (Hartree)	-609.2650	-708.5001	-807.7340	-946.2982	-1283.3304
E_2 (Hartree)	-609.1499	-708.3496	-807.5471	-946.0751	-1283.0004
E_2' (Hartree)	-609.1679	-708.3671	-807.5650	-946.0947	-1283.0204
E_1+E_2'-E_2 (Hartree)	-609.2829	-708.5176	-807.7519	-946.3178	-1283.3504
			n-octanol		
E_1 (Hartree)	-609.2649	-708.5000	-807.7339	-946.2981	-1283.3302
E_2 (Hartree)	-609.1498	-708.3495	-807.5471	-946.0749	-1283.0003
E_2' (Hartree)	-609.1674	-708.3663	-807.5642	-946.0928	-1283.0171
E_1+E_2'-E_2 (Hartree)	-609.2824	-708.5168	-807.7510	-946.3159	-1283.3471
log(Poctanol/Pwater)	0.23	0.37	0.41	0.87	1.52

E_1=single point energy, E_2=solvent energy (structure), E_2'=solvent energy (structure+solvent)

S5. Synthesis and characterization of $2CF_3$-UiO-66 devices

S5.1. Synthesis of $2CF_3$-UiO-66@CT/SP.

$ZrCl_4$ (0.0233 g, 0.1 mmol), 2,5-bis(trifluoromethyl)terephthalic acid (0.0302 g, 0.1 mmol), and benzoic acid (0.0122 g, 0.1 mmol) were completely dissolved in DMF (6 mL/8 mL) in a reaction kettle lined with polytetrafluoroethylene containing. The pretreated cotton/sponge was immersed in the solution. The reaction kettle was sealed and heated to 100 °C for 24 hours in an oven. Then, the reaction was programmablely cooled down to 25 °C within 6 hours. Then, the cotton/sponge composite materials were washed with ethanol to remove excess MOFs on the surface and dried under vacuum (Figure S36, S37).

Figure S36. Natural cotton (left) and synthetic $2CF_3$-UiO-66@CT (right) composites

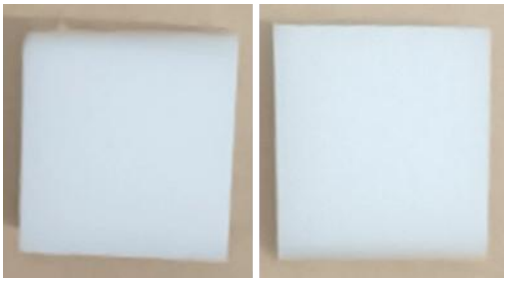

Figure S37. Sponge (left) and synthetic $2CF_3$-UiO-66@SP (right) composites

S5.2. Energy dispersive X-ray spectroscopy (EDX) characterization.

Choose a small amount of natural cotton fiber/ sponge, and composite materials are stuck with conductive adhesive on a copper sample holder. The materials were sprayed with gold before testing.

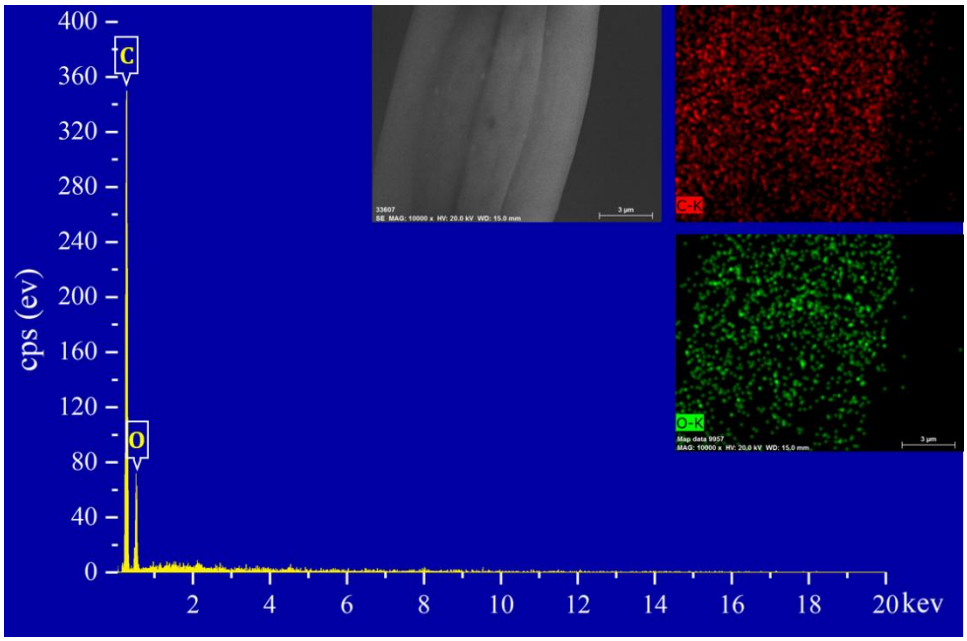

Figure S38. SEM image (top left) and element distribution of cotton fiber and EDX.

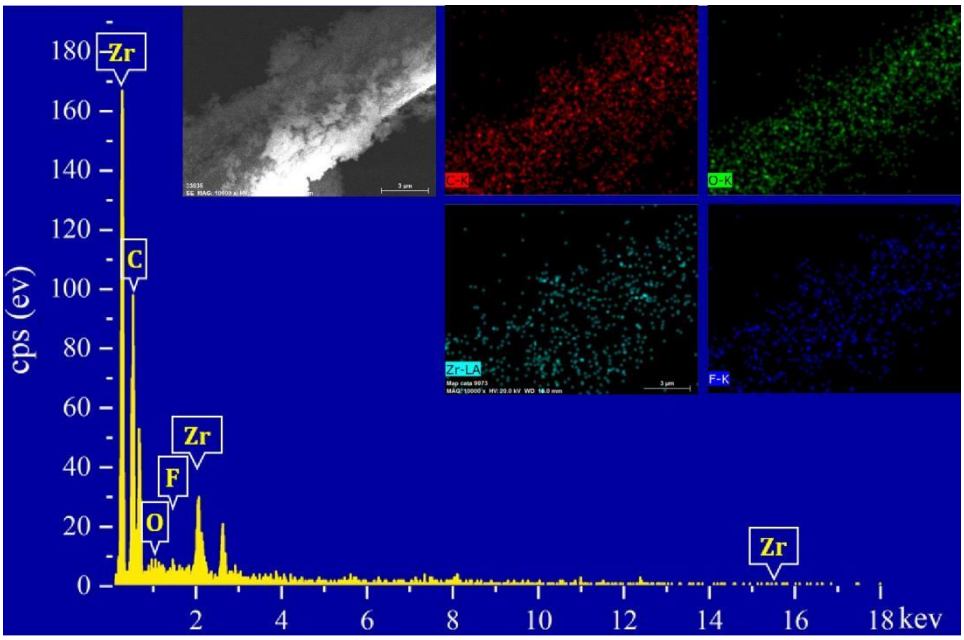

Figure S39. SEM image (top left) and element distribution of $2CF_3$-UiO-66@CT and EDX.

Table S2. Element content of Cotton Fiber

Element	Elemental (wt %)
C	69.56
O	30.44

Table S3. Element content of $2CF_3$-UiO-66@CT

Element	Elemental (wt %)
C	47.45
O	31.51
F	16.43
Zr	4.61

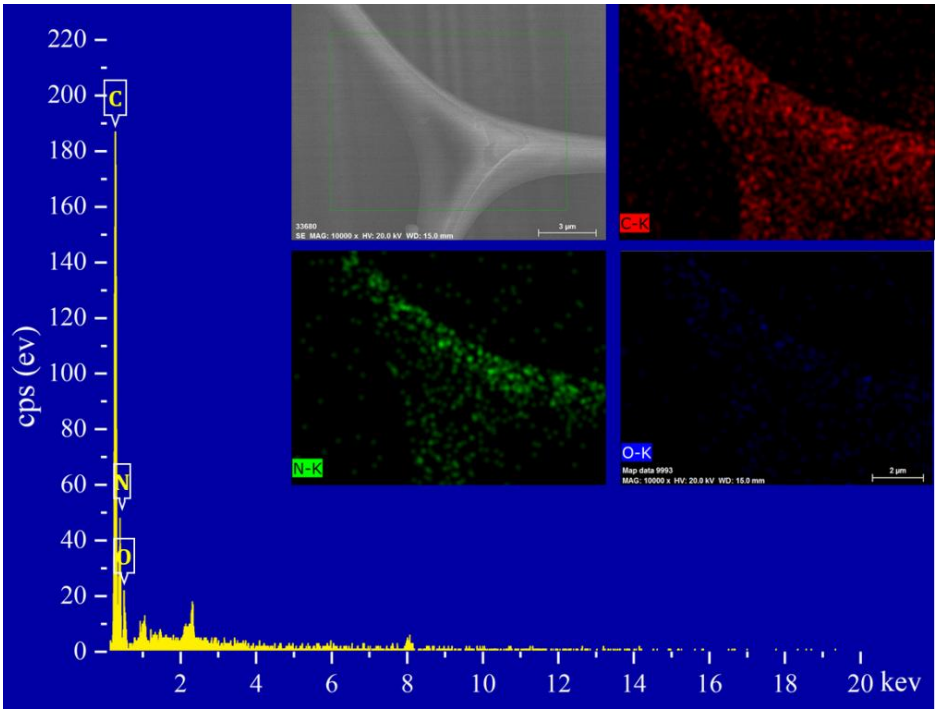

Figure S40. SEM image (top left) and element distribution of sponge and EDX.

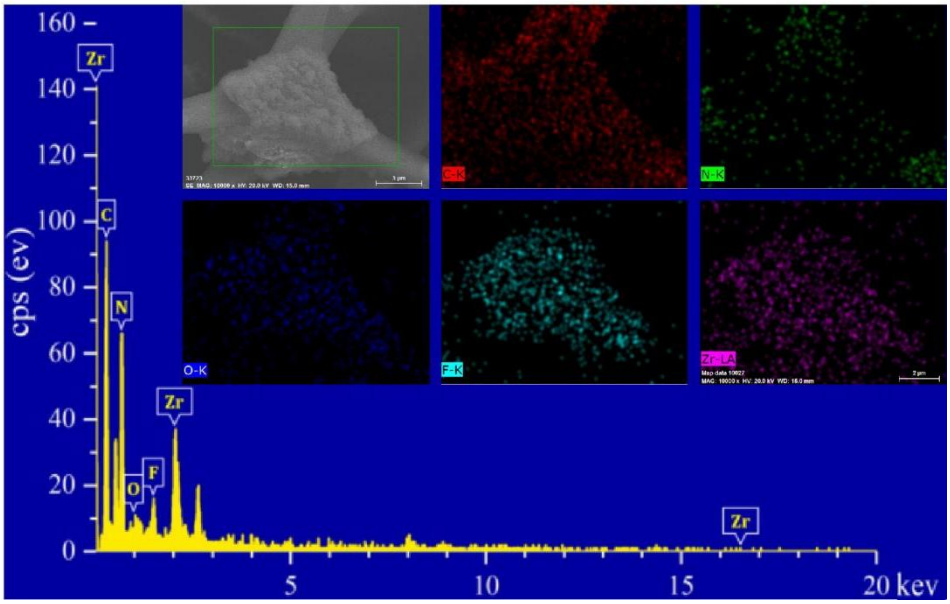

Figure S41. SEM image (top left) and element distribution of $2CF_3$-UiO-66@SP and EDX.

Table S4. Element content of the sponge

Element	Elemental (wt %)
C	40.95
N	46.05
O	13.00

Table S5. Element content of $2CF_3$-UiO-66@SP

Element	Elemental (wt %)
C	40.18
N	9.17
O	17.27
F	25.41
Zr	7.98

S5.3. PXRD characterization of $2CF_3$-UiO-66@CT/SP.

The $2CF_3$-UiO-66@CT/SP composite material is placed on the sample slot, and the measuring range of 5-80° is selected for direct measurement.

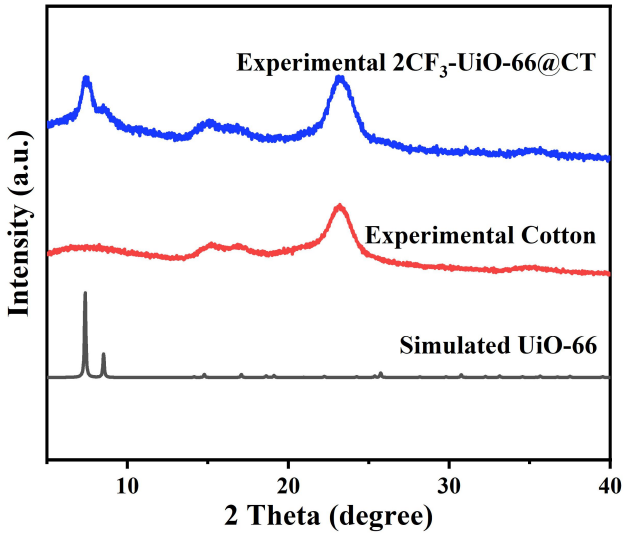

Figure S42. PXRD profiles simulated UiO-66 and experimental data of cotton and $2CF_3$-UiO-66@CT

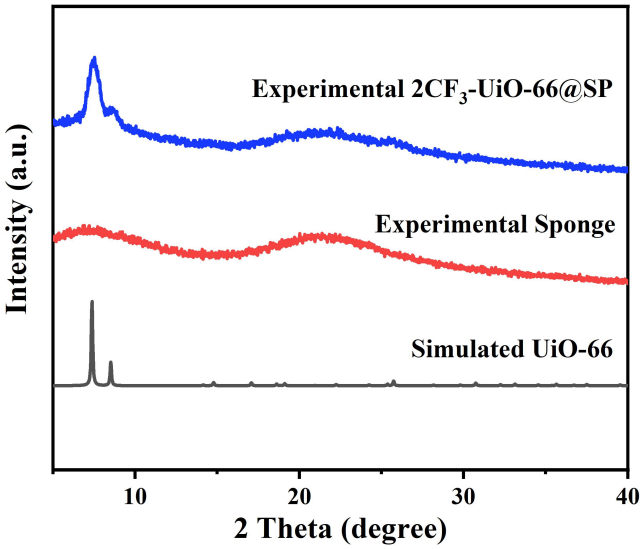

Figure S43. PXRD profiles simulated UiO-66 and experimental data of cotton and $2CF_3$-UiO-66@SP

S5.4. FT-IR characterization of composite materials.

A small amount of natural cotton fiber and composite cotton fiber were mixed with KBr and pressed to prepare samples. The test range is 4000-500 cm^{-1}.

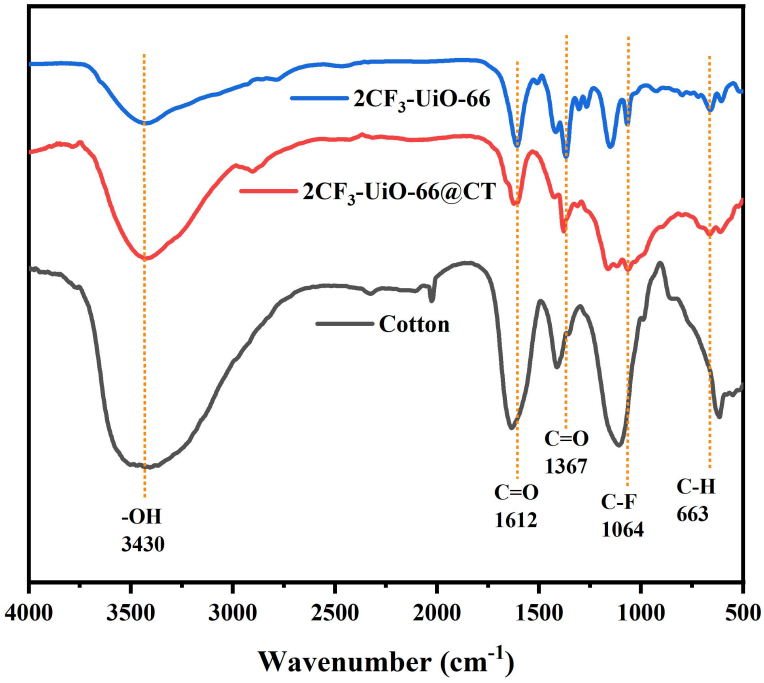

Figure S44. FT-IR of cotton fiber, 2CF_3-UiO-66@CT, and 2CF_3-UiO-66

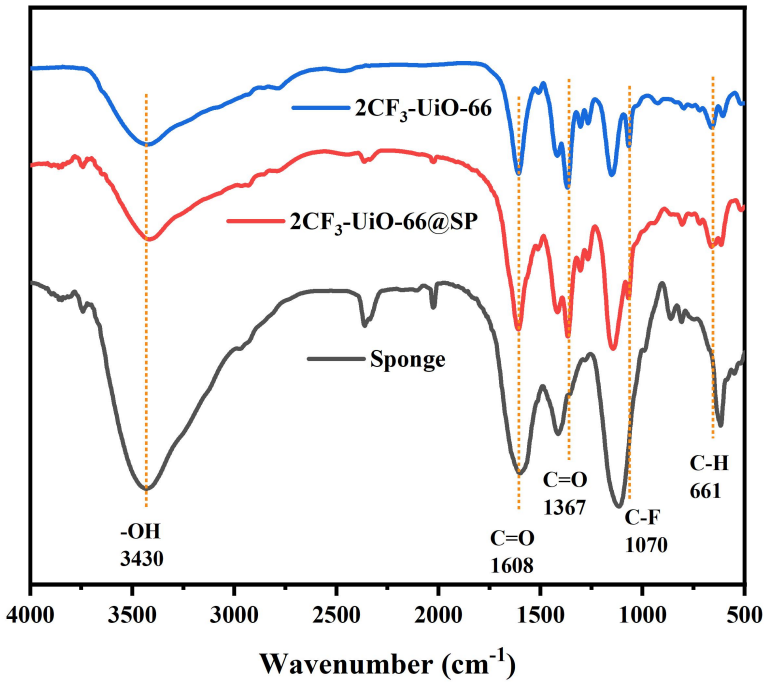

Figure S45. FT-IR of sponge, 2CF_3-UiO-66@SP, and 2CF_3-UiO-66

S5.5. The water contact angle measurement of $2CF_3$-UiO-66@CT/SP.

The $2CF_3$-UiO-66@CT/SP material is directly placed on the water contact angle tester, and the water droplets fall about 5 μL each time.

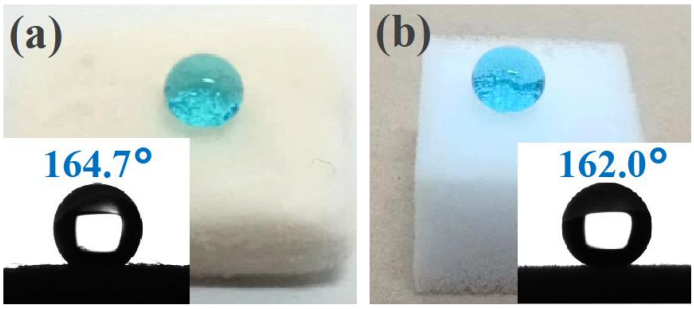

Figure S46. Images of water contact angle of (a) $2CF_3$-UiO-66@CT and (b) $2CF_3$-UiO-66@SP.

S5.6. The rolling test of water droplets is on $2CF_3$-UiO-66@CT/SP.

The $2CF_3$-UiO-66@CT/SP material is placed at a position of 30° on the horizontal plane, and the water droplets dyed with methylene blue are dropped on the composite.

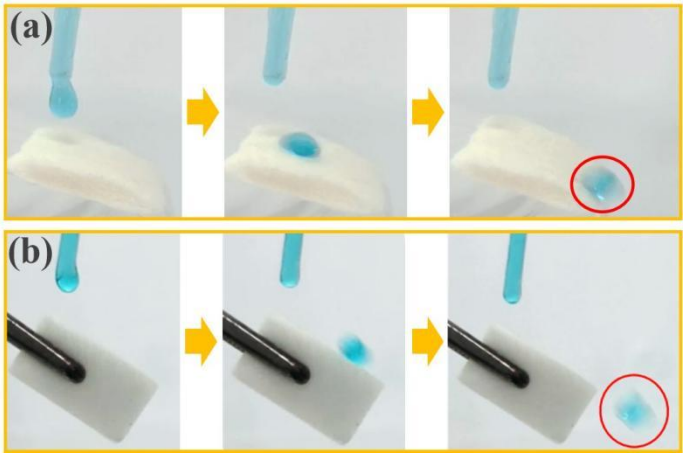

Figure S47. Images of water rolling on (a) $2CF_3$-UiO-66@CT and (b) $2CF_3$-UiO-66@SP.

S5.7. Hydrophobicity Test of $2CF_3$-UiO-66@CT/SP in water

Place $2CF_3$-UiO-66@CT/SP above the water surface, press it under the water surface with an external force, and then withdraw the external force.

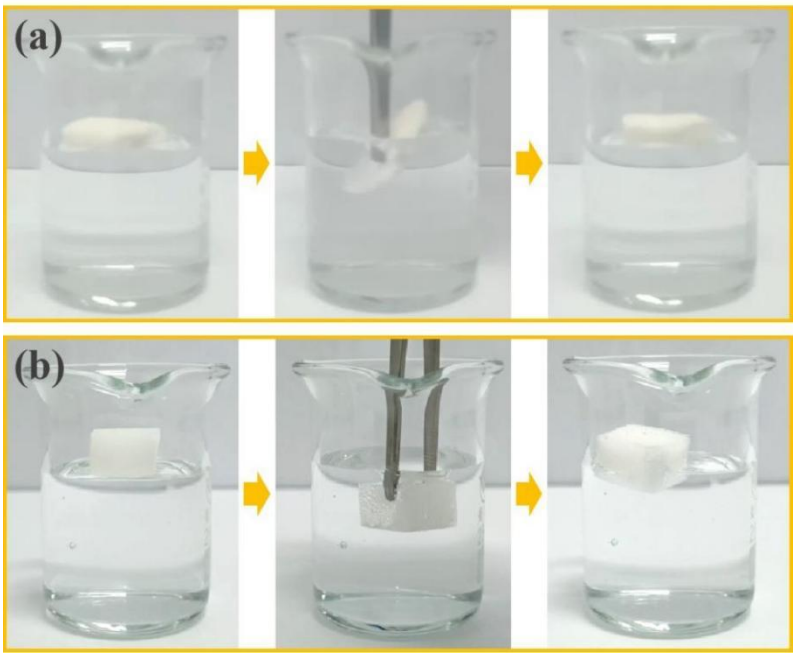

Figure S48. Images of immersing (a) $2CF_3$-UiO-66@CT and (b) $2CF_3$-UiO-66@SP in water.

S6. Oil-water separation performance of $2CF_3$-UiO-66 devices

S6.1. Removing a small amount of oil from the water

S6.1.1. $2CF_3$-UiO-66@CT composite material removes a small amount of oil from water

Toluene (0.5 mL, with Sudan I as the indicator) was mixed with 20 mL of deionized water. The obtained $2CF_3$-UiO-66@CT was added to the solution, and toluene was absorbed by the composite material, effectively separating it from the water. Upon treatment with the composite cotton material, the oil-water mixture became clear, with no visible oil residue. Similarly, carbon tetrachloride (0.5 mL) was mixed with 20 mL of deionized water. When the $2CF_3$-UiO-66@CT was immersed in water, it quickly absorbed carbon tetrachloride. The surface of the composite cotton material without adsorbed heavy oil remains dry. These results demonstrate the material's ability to selectively adsorb heavy oil, as evidenced by the absence of visible oil compounds at the bottom of the treated oil-water mixture (Figure S49).

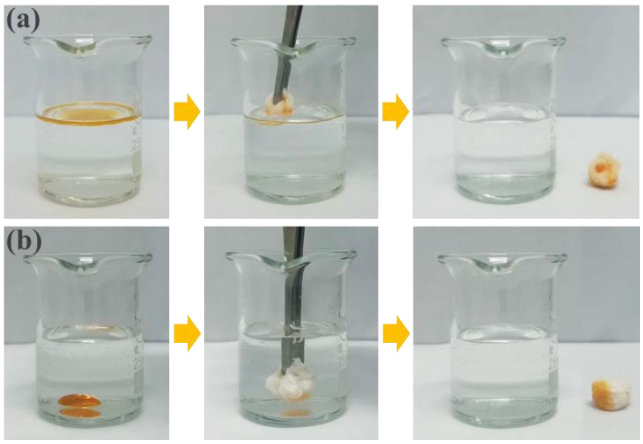

Figure S49. Images of 2CF_3-UiO-66@CT composites adsorb a small amount of (a) toluene (0.5 mL) and (b) tetrachloride carbon (0.5 mL) from water (20 mL).

S6.1.2. 2CF_3-UiO-66@SP composite material removes a small amount of oil from water

Using the same method of 2CF_3-UiO-66@CT, 2CF_3-UiO-66@SP was used to adsorb toluene and tetrachloride in water. The part of the composite sponge surface without adsorbed oil compounds remains dry, indicating the material's efficient and selective oil adsorption capability. After treatment with the composite sponge material, the oil-water mixture shows no visible oil compounds in the water (Figure S50).

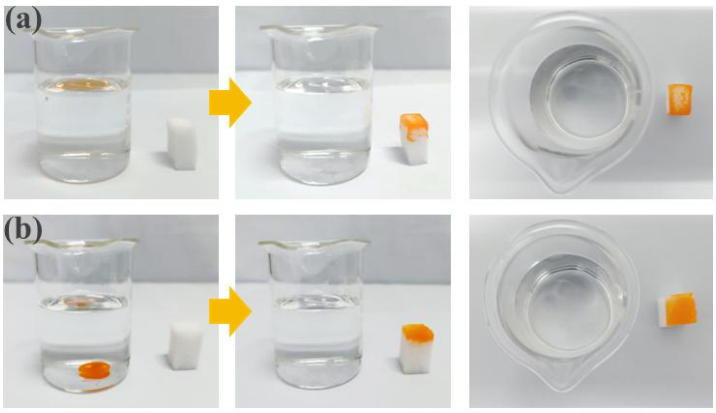

Figure S50. Images of 2CF_3-UiO-66@SP composites adsorb a small amount of (a) toluene (0.5 mL) and (b) tetrachloride carbon (0.5 mL) from water (20 mL).

S6.2. Oil adsorption test

S6.2.1. The oil adsorption capacity of 2CF_3-UiO-66@CT

The measurement was repeated 5 times. The average adsorption capacities of dichloromethane, chloroform, carbon tetrachloride, toluene, petroleum ether, n-hexane, hexadecane, kerosene, and gasoline are calculated 9.92 ± 0.43 $g \cdot g^{-1}$, 11.90 ± 0.23 $g \cdot g^{-1}$, 14.01 ± 0.35 $g \cdot g^{-1}$, 8.06 ± 0.32 $g \cdot g^{-1}$, 6.27 ± 0.45 $g \cdot g^{-1}$, 6.36 ± 0.26 $g \cdot g^{-1}$, 6.85 ± 0.44 $g \cdot g^{-1}$, 8.56 ± 0.34 $g \cdot g^{-1}$, 7.39 ± 0.30 $g \cdot g^{-1}$, respectively. However, the average adsorption capacity for water is only

0.05 ± 0.02 $g \cdot g^{-1}$, which indicates that the composite cotton material has good lipophilic and hydrophobic ability and is an ideal adsorption material (Figure S51 a). The curve in Figure S51 b indicates a positive correlation ($R^2 > 0.94$) between the adsorption capacity of organic solvents and their density (Table S6).

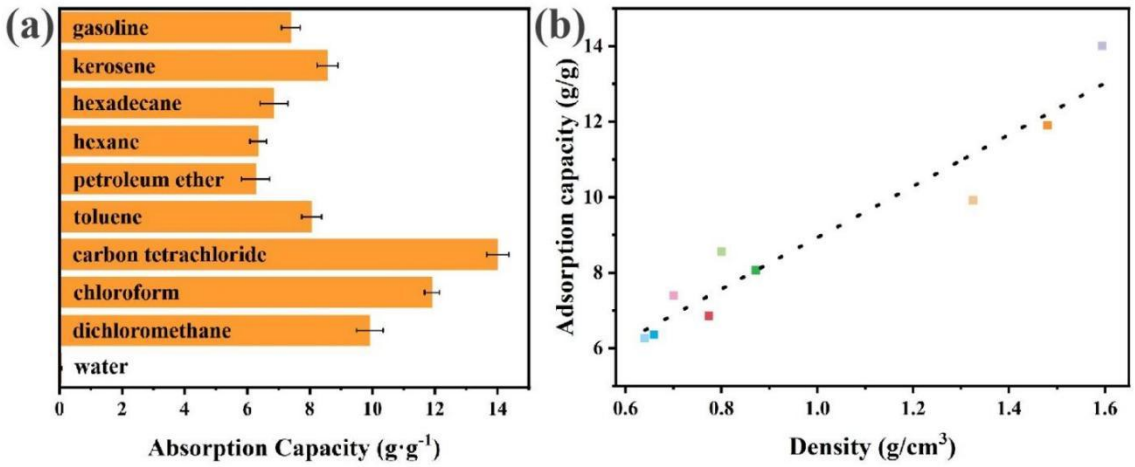

Figure S51. (a) The adsorption capacity of dichloromethane, chloroform, carbon tetrachloride, toluene, petroleum ether, n-hexane, hexadecane, kerosene, and gasoline. (b) The linear fit of the adsorption capacity and density of different organic solvents for $2CF_3$-UiO-66@CT.

Table S6. The linear fit result of the adsorption capacity and density of different organic solvents for $2CF_3$-UiO-66@CT.

Equation	y = a + b*x
Intercept	5.21 ± 8.08
Slope	89.87 ± 7.74
Residual sum of squares	473.65
R^2	0.94

S6.2.2. The oil adsorption capacity of $2CF_3$-UiO-66@SP

Through the same method, the average adsorption capacities of dichloromethane, chloroform, carbon tetrachloride, toluene, petroleum ether, n-hexane, hexadecane, kerosene, gasoline for $2CF_3$-UiO-66@SP are measured as 139.69 ± 2.50 $g \cdot g^{-1}$, 136.35 ± 3.65 $g \cdot g^{-1}$, 141.52 ± 2.53 $g \cdot g^{-1}$, 78.98 ± 2.19 $g \cdot g^{-1}$, 70.76 ± 2.97 $g \cdot g^{-1}$, 64.58 ± 2.12 $g \cdot g^{-1}$, 77.23 ± 2.67 $g \cdot g^{-1}$, 68.35 ± 2.75 $g \cdot g^{-1}$, 64.15 ± 2.65 $g \cdot g^{-1}$, respectively. The average adsorption capacity for water is 0.15 ± 0.02 $g \cdot g^{-1}$, which is an ideal adsorption material and has good lipophilic and hydrophobic ability (Figure S52 a). Through the characterization of the fitting curve, there is a positive correlation

between the adsorption capacity of different organic solvents and their densities (Figure S52 b). R^2 is more than 0.91 (Table S7).

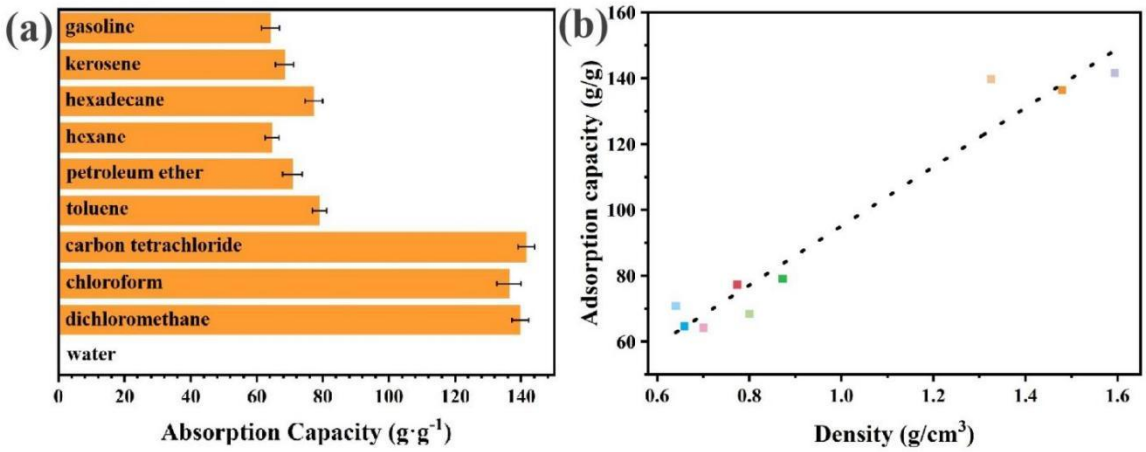

Figure S52. (a)The adsorption capacity of dichloromethane, chloroform, carbon tetrachloride, toluene, petroleum ether, n-hexane, n-hexadecane, kerosene, and gasoline. (b) The linear fit of the adsorption capacity and density of different organic solvents for $2CF_3$-UiO-66@SP.

Table S7. The linear fit result of the adsorption capacity and density of different organic solvents for $2CF_3$-UiO-66@SP.

Equation	y = a + b*x
Intercept	2.12 ± 0.77
Slope	6.81 ± 0.74
Residual sum of squares	4.28
R^2	0.91

S6.3. Oil-water separation efficiency of $2CF_3$-UiO-66@CT/SP

The $2CF_3$-UiO-66@CT composites separated by oil and water can recover some of the adsorbed oil compounds by mechanical extrusion, rinse and dry with ethanol three times, and then recycle them again. The average oil-water separation efficiency of dichloromethane, chloroform, carbon tetrachloride, toluene, petroleum ether, n-hexane, hexadecane, kerosene, and gasoline for $2CF_3$-UiO-66@CT are measured as 99.62 ± 0.14 %, 99.19 ± 0.52 %, 99.47 ± 0.35 %, 99.49 ± 0.11 %, 98.94 ± 0.64 %, 99.27 ± 0.66 %, 99.47 ± 0.23 %, 99.66 ± 0.10 %, 99.61 ± 0.15 %, respectively.

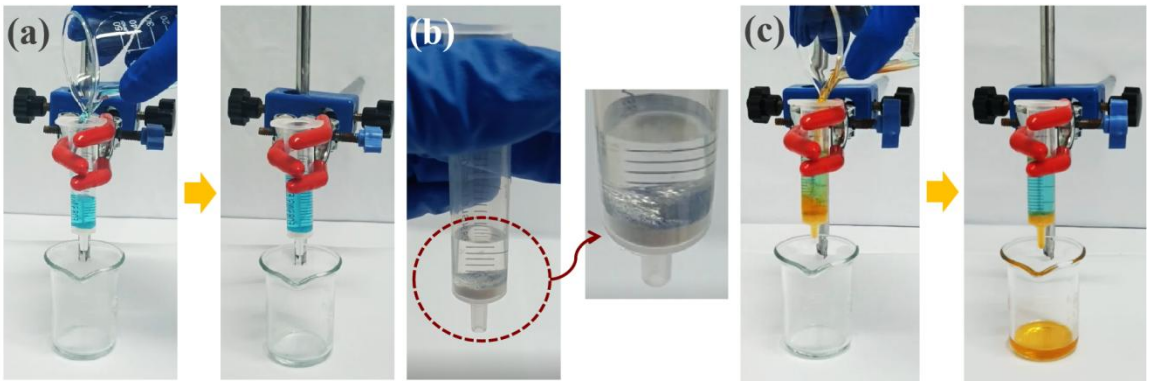

Figure S53. Oil-water separation test of $2CF_3$-UiO-66@CT

The device for preparing $2CF_3$-UiO-66@SP composite material is the same as $2CF_3$-UiO-66@CT composite material. The average oil-water separation efficiency of dichloromethane, chloroform, carbon tetrachloride, toluene, petroleum ether, n-hexane, hexadecane, kerosene, and gasoline for $2CF_3$-UiO-66@SP are measured as 95.89 ± 0.65 %, 98.06 ± 0.89 %, 98.96 ± 0.45 %, 98.51 ± 0.21 %, 98.62 ± 0.46 %, 98.77 ± 0.32 %, 98.15 ± 0.42 %, 99.02 ± 0.36 %, 97.66 ± 0.82 %, respectively.

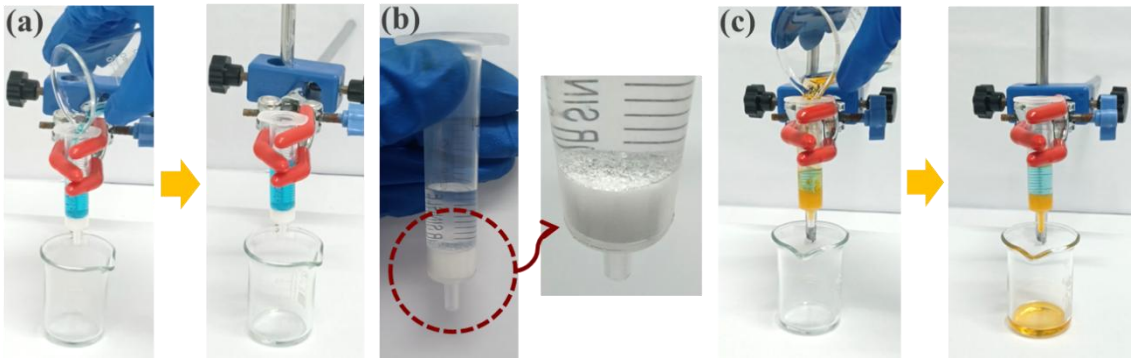

Figure S54. Oil-water separation test of $2CF_3$-UiO-66@SP

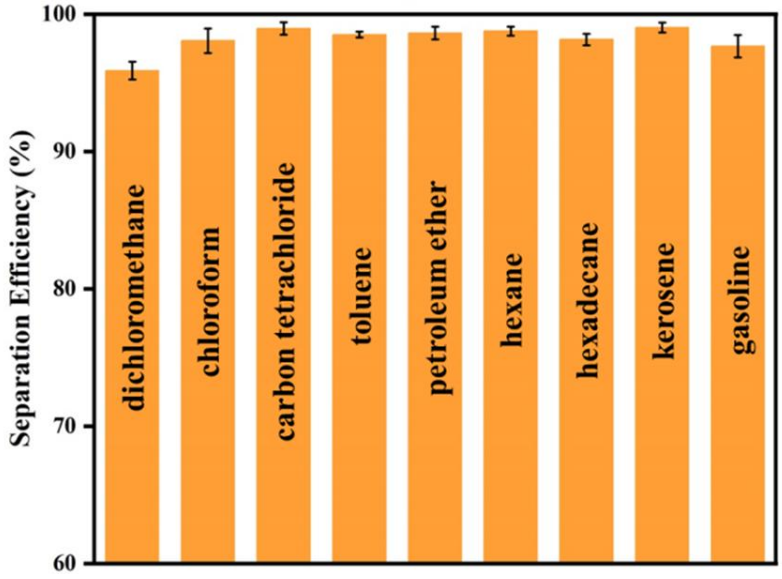

Figure S55. The oil-water separation efficiency of $2CF_3$-UiO-66@SP

S6.4. Water content measurement

A piece of composite cotton is placed in the needle position of the 5 mL syringe and compacted to make a simple oil-water separation device. Mix 92 gasoline (98% carbon tetrachloride) from 60 mL with deionized water from 3 mL and slowly pour the mixed solution into the oil-water separation unit until the mixed solution is completely poured out. The oil phase will flow into the beaker through the composite cotton, and the water phase will be intercepted above the composite cotton to determine the water content of the oil phase in the beaker. The resulting data are shown in Table 2, S8.

Table S8. Determination of water content of carbon tetrachloride after water–oil separation

NO.	Sample	Water content (%)
1	98% carbon tetrachloride	**0.0112**
2	the mixed solution was separated once by $2CF_3$-UiO-66@CT material	0.0078
3	the mixed solution was separated three times by $2CF_3$-UiO-66@CT material	0.0072

S6.5. Effect of different water environments on oil-water separation of $2CF_3$-UiO-66@CT/SP in practical application

We also investigated the effect of different water environments on oil-water separation efficiency in practical application. We selected 3.5% simulated seawater and Inner Mongolia University's (IMU) TaoLi lake water as the consideration solution for the water environment and

tested the oil-water separation efficiency of $2CF_3$-UiO-66@CT and $2CF_3$-UiO-66@SP composites. Carbon tetrachloride is used as heavy oil in separation, and the separation efficiency is shown in the column chart of Figure S58. The separation efficiency of $2CF_3$-UiO-66@CT composite material is 99.21 ± 0.26 % in the simulated seawater environment and 99.29 ± 0.13 % in the Inner Mongolia University's TaoLi lake environment. The separation efficiency of $2CF_3$-UiO-66@SP composite material is 98.66 ± 0.31 % in the simulated seawater environment and 98.27 ± 0.26 % in Inner Mongolia University's TaoLi lake environment. Under the influence of man-made measurement error, there is not much difference compared with the previous deionized water data, which can prove that $2CF_3$-UiO-66@CT composite and $2CF_3$-UiO-66@SP composite have excellent oil-water separation efficiency in practical application.

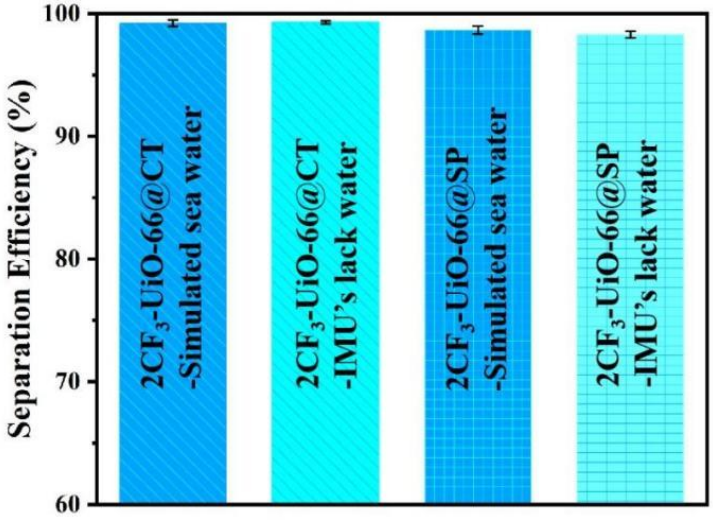

Figure S56. The oil-water separation efficiency of $2CF_3$-UiO-66@CT/SP in different water quality.

S6.6. Speed measurement of oil-water separation.

To measure the speed of separating the oil-water mixture of our synthetic $2CF_3$-UiO-66@CT composites, we have made a set of oil-water separation devices. The PVC adapter is combined with two transparent PVC tubes with a diameter of 3.4 cm, and the $2CF_3$-UiO-66@CT composite material is installed at the adapter to form a straight pipe device, as shown in Figure S57. The mixture of dichloromethane and water is separated by gravity drive. Under the constant pressure of 165 mm water injection, the time of 200 mL dichloromethane flowing through the composite cotton material was tested. The experiment was repeated three times. Using unit volume velocity to calculate the velocity of oil passing through $2CF_3$-UiO-66@CT composite material in an oil-water mixture

$$v = V / t \quad (2)$$

In the formula, v is the flow rate of oil in the oil-water mixture, in units of $cm^3 \cdot s^{-1}$, and V is the liquid volume of dichloromethane, in cm^3; t for time, in s.

The average flow time of 200 cm^3 dichloromethane through the composite cotton material was 18.4 s, and the average flow velocity was 10.87 cm^3/s.

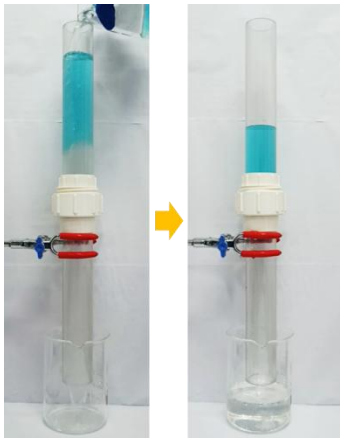

Figure S57. Images of the device for the oil-water separation speed measurement.

S6.7. Anti-gravity extraction.

The anti-gravity extraction experiment of the 2CF_3-UiO-66@SP composite sponge was carried out (Figure S58). And 7.5 mL of carbon tetrachloride (dyed by Sudan I) and deionized water (dyed by methylene blue) were added to the test tube. Put the 2CF_3-UiO-66@SP composite material to the end of the tube. Because of the superhydrophobicity, the composite material will not absorb water in the anti-gravity extraction process. Only oil can pass through the composite material, and water is surrounded by the device. After adsorbing the oil compounds, the UiO-66@SP composite was removed from the test tube. The obtained oil was squeezed out into another beaker.

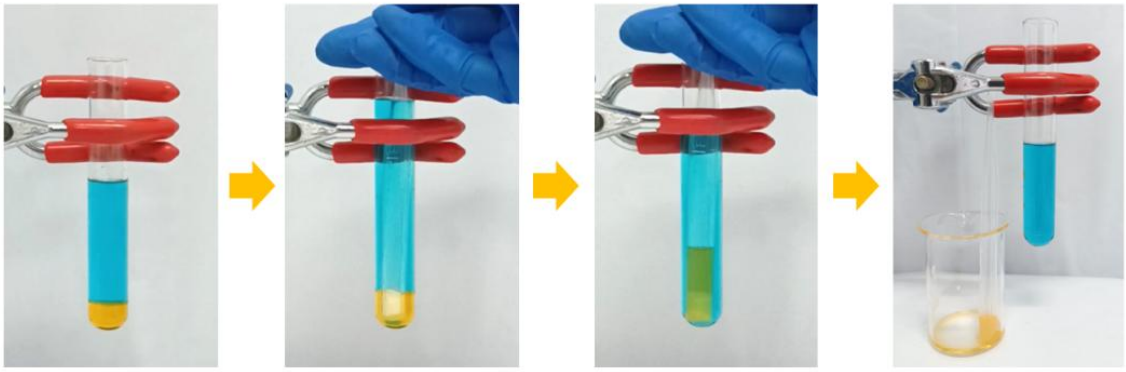

Figure S58. Anti-gravity extraction of 2CF_3-UiO-66@SP composite materials

Table S9. 2CF_3-UiO-66@CT limiting oxygen index

Sample	LOI (%)
Cotton	18.5
2CF_3-UiO-66@CT	23.5

S7. Stability of $2CF_3$-UiO-66@CT/SP

S7.1. Solvent stability characterization of composite materials.

The $2CF_3$-UiO-66@CT/SP material was soaked in gasoline, toluene, and carbon tetrachloride of 4 mL for 24 hours, and the composite was dried for PXRD test.

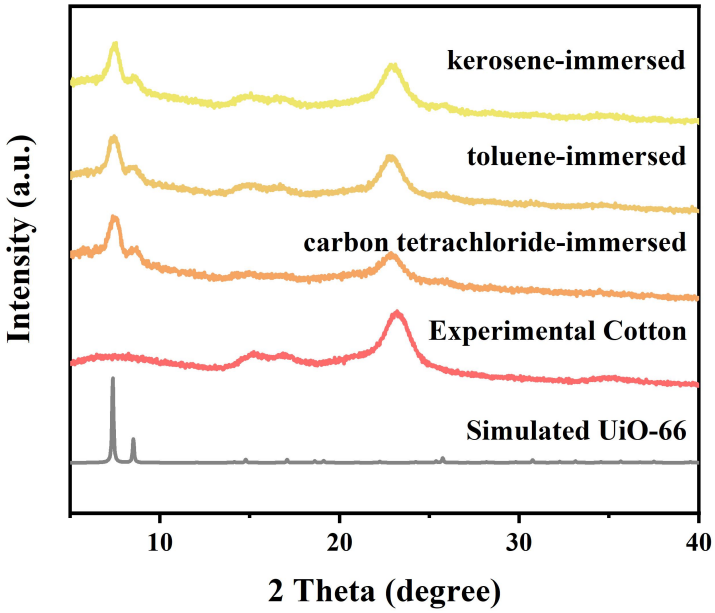

Figure S59. PXRD profiles of simulated UiO-66 and experimental data of cotton, $2CF_3$-UiO-66@CT after immersing in carbon tetrachloride, toluene, and kerosene for 24 h.

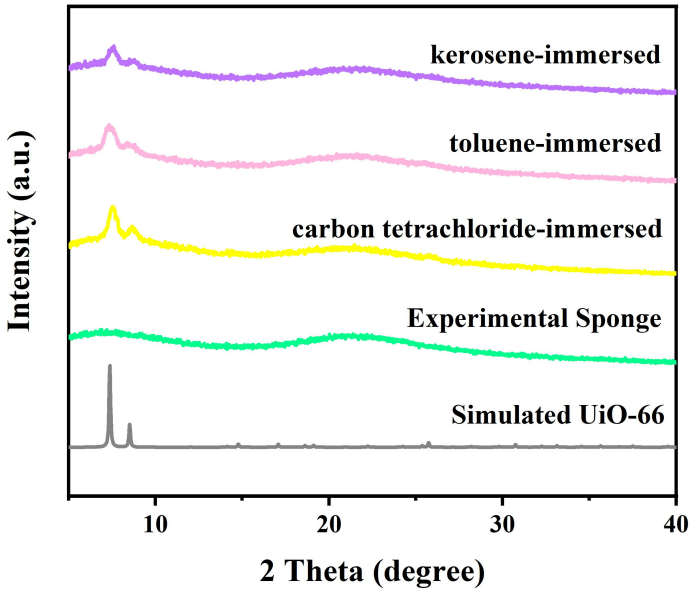

Figure S60. PXRD profiles of simulated UiO-66 and experimental data of sponge $2CF_3$-UiO-66@SP after immersing in carbon tetrachloride, toluene, and kerosene for 24 h.

S7.2. Water stability test.

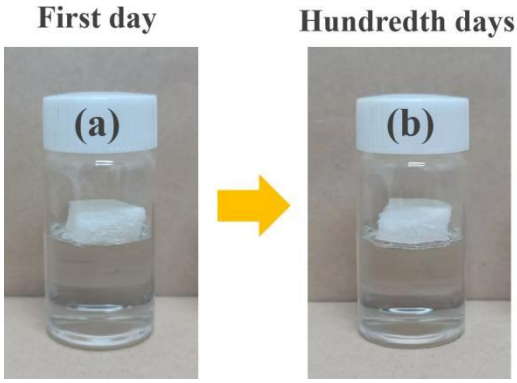

Figure S61. Images of putting 2CF$_3$-UiO-66@CT on DI water for 100 days.

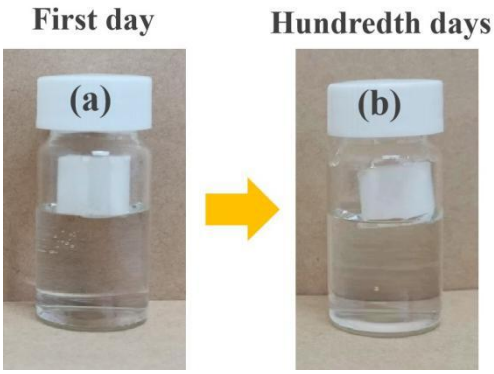

Figure S62. Images of putting 2CF$_3$-UiO-66@SP on DI water for 100 days.

S7.3. Mechanical stability and boiling water stability characterization of composite materials.

Compression test: The 2CF$_3$-UiO-66@CT/SP was cyclically compressed 5 times with 50% compressive deformation. The weight loss changes of 2CF$_3$-UiO-66@CT/SP before and after testing are shown in Table S10.

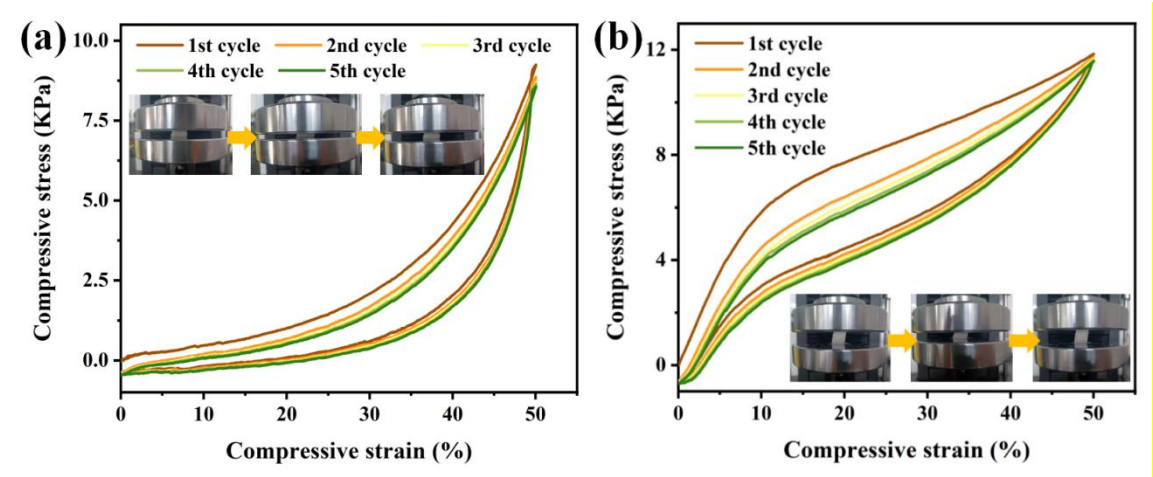

Figure S63. Compression test of (a) 2CF$_3$-UiO-66@CT and (b) 2CF$_3$-UiO-66@SP.

Stretching test: $2CF_3$-UiO-66@CT was cut to a cross-sectional size of 1.7 cm × 0.2 cm. The weight loss changes of $2CF_3$-UiO-66@CT before and after testing are shown in Table S10.

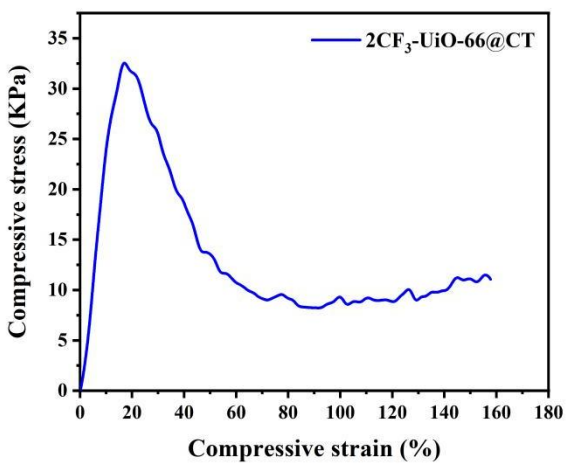

Figure S64. Stretching test of $2CF_3$-UiO-66@CT.

Abrasion test: The $2CF_3$-UiO-66@CT/SP composite was placed on 1200 mesh sandpaper, and then a 20 g object was taken and pressed on the surface of the composite and dragged at a speed of 2 cm/s for about 1 m. The weight loss changes of $2CF_3$-UiO-66@CT/SP before and after testing are shown in Table S10.

Boiling water test[12]: $2CF_3$-UiO-66@CT/SP composite was placed in boiling water and kept for 30 min. The composite material is still floating above the water. The weight loss changes of $2CF_3$-UiO-66@CT/SP before and after testing are shown in Table S10.

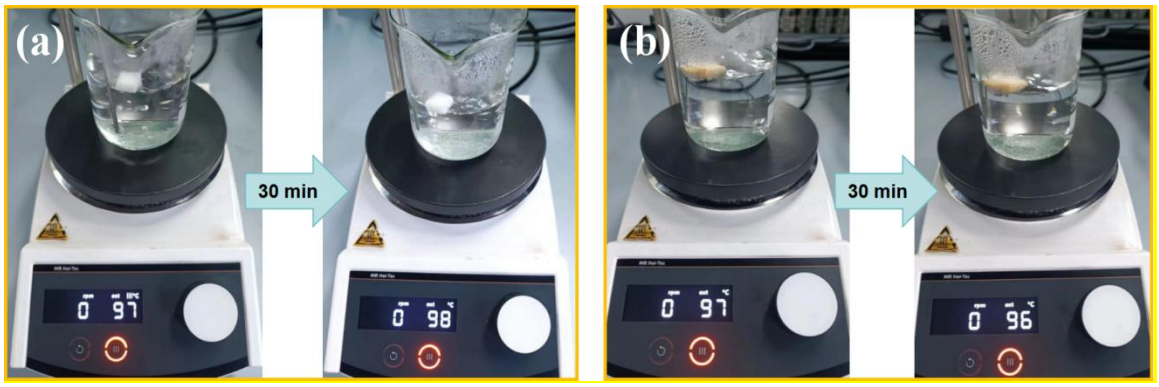

Figure S65. Images of (a) $2CF_3$-UiO-66@CT and (b) $2CF_3$-UiO-66@SP

The average oil-water separation efficiency of carbon tetrachloride for $2CF_3$-UiO-66@CT after stress, abrasion, stretch and boiling water test are measured as 99.39 ± 0.23%, 99.38 ± 0.32%, 99.32 ± 0.25%, 99.27 ± 0.42%. There is no great change compared with the original 99.47 ±0.35%.

The average oil-water separation efficiency of carbon tetrachloride for 2CF$_3$-UiO-66@SP after stress, abrasion and boiling water test are measured as 98.68 ± 0.44%, 98.75 ± 0.33%, 98.24 ± 0.22%. There is no great change compared with the original 98.96 ± 0.52%.

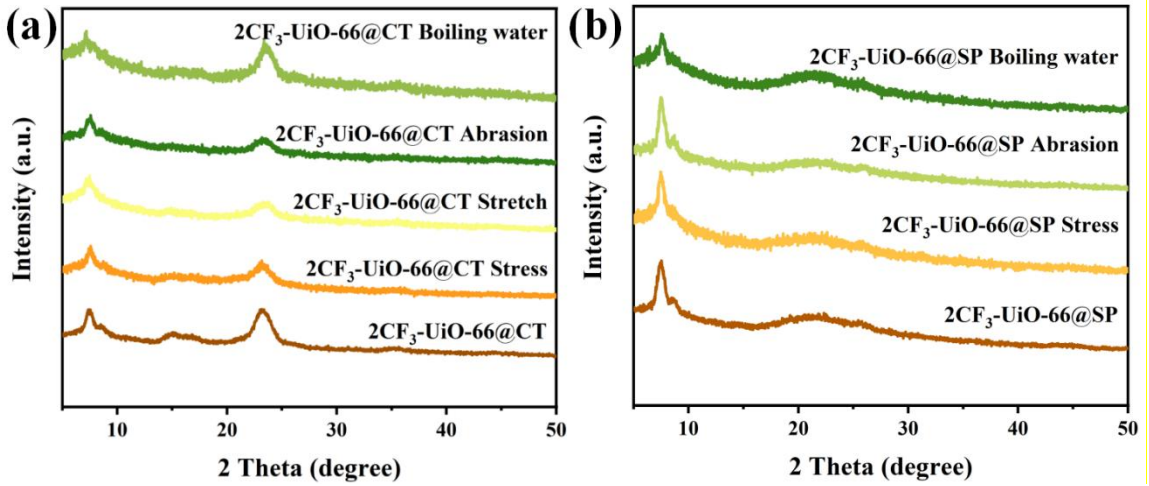

Figure S66. PXRD profiles of (a) 2CF$_3$-UiO-66@CT and (b) 2CF$_3$-UiO-66@SP after mechanical stability test and boiling water stability test.

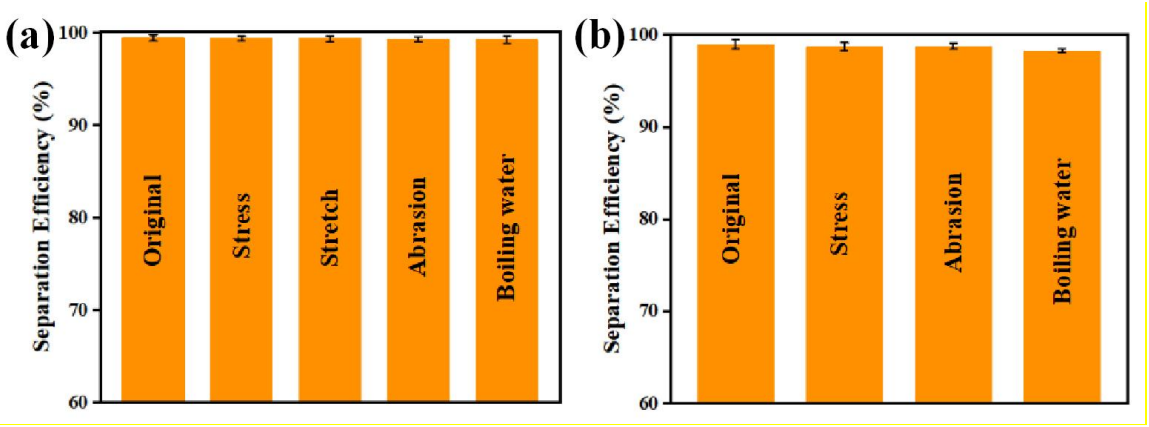

Figure S67. The oil-water separation efficiency of (a) 2CF$_3$-UiO-66@CT and (b) 2CF$_3$-UiO-66@SP after mechanical stability test and boiling water stability test.

Table S10. Weight changes of different materials after mechanical tests and boiling water

	2CF$_3$-UiO-66@CT	cotton	2CF$_3$-UiO-66@SP	sponge
Stress	0	0	0	0
Stretch	0.52%	0.55%	-	-
Abrasion	2.85%	2.77%	5.76%	0
Boiling water	5.53%	3.92%	4.78%	5.43%

S7.4. $2CF_3$-UiO-66@CT cycle test method.

The $2CF_3$-UiO-66@CT composites separated by oil and water can recover some of the adsorbed oil compounds by mechanical extrusion, rinse and dry with ethanol and recycle them again.

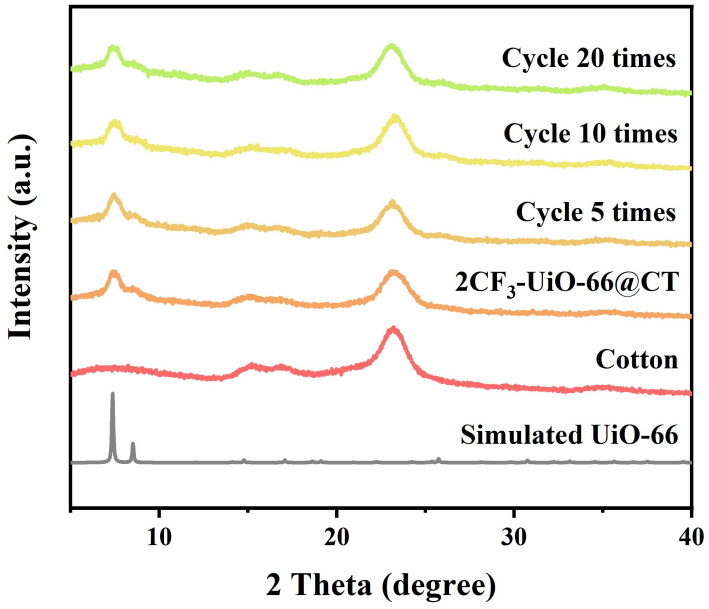

Figure S68. PXRD profiles of $2CF_3$-UiO-66@CT after filtering carbon tetrachloride for different cycles

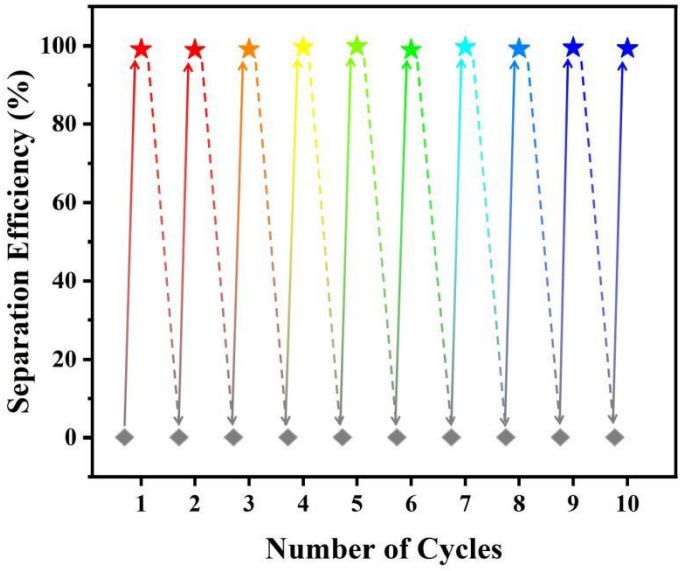

Figure S69. The separation efficiency of $2CF_3$-UiO-66@CT after filtering carbon tetrachloride for different cycles

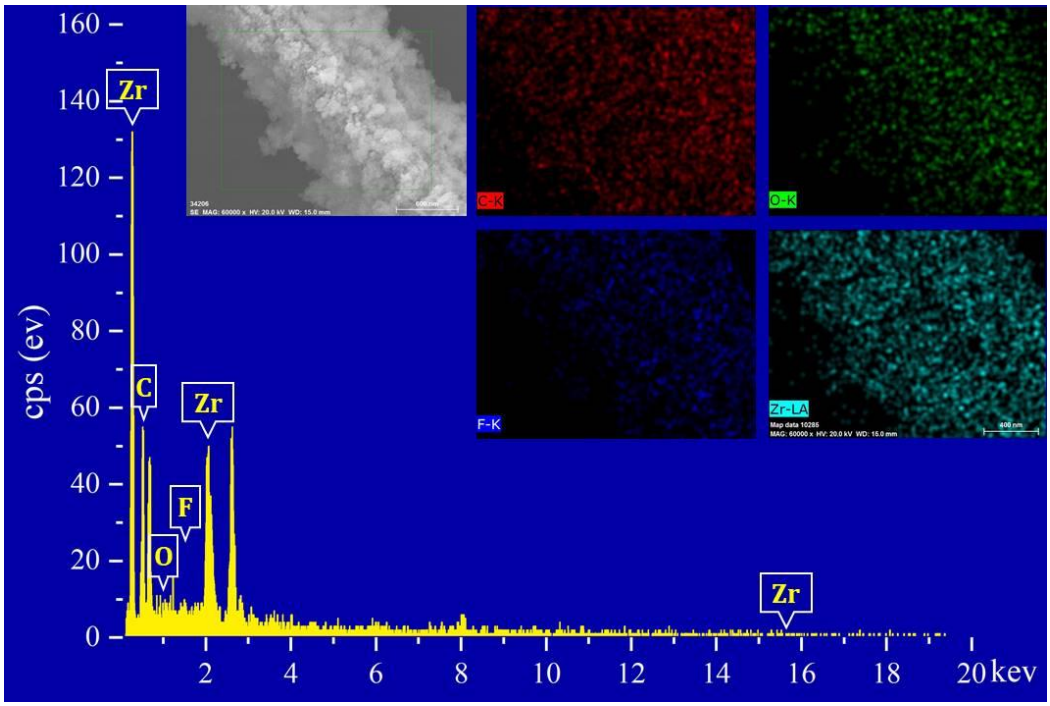

Figure S70. SEM image (top left) and element distribution of $2CF_3$-UiO-66@CT after Ten cycles (top right) and EDX.

Table S11. The element content of $2CF_3$-UiO-66@CT before and after ten cycles of water–oil separation.

Element	Elemental (wt %) before adsorption	Elemental (wt %) after adsorption
C	47.45	54.79
O	31.51	19.19
F	16.43	17.05
Zr	4.61	8.96

Table S12. Oil-water separation properties of hydrophobic MOF complex fibers

MOF complexes's name	WCA (°)	Separation Efficiency (%)	References
Ti-MOFs/cotton fibers	154.7	98.5	13
SH-UiO-66@CFs	163	95	14
SHMOF- polypropylene	160	95-99	15
ZIF-8/cotton fabrics	155	98.6	16
cotton/ZIF-8@PDMS	151.36	98	17
ZIF-8@Kevlar	152.2	98	18
SMCF	168.4	\	19
PZCF	142.8	\	20
2CF_3-UiO-66@CT	164.7	99.4	This work

Table S13. Comparative adsorption capacities of various MOF complex sponges for oil adsorption.

MOF complexes's name	WCA (°)	Adsorption Capacity (g/g)	References
Si@PBA@PDA@MS	163.5	53.4-97.5	21
FPUF@MOF-LDH@HTMS	153	42-73	22
PDMS/CuTPA/PU	157	10-33	23
FPUF/BN@MOF-LDH @APTES	121	18-33	24
ZIF-8/RGO/PU	125	15-35	25
Fe_3O_4 @GO@OTS/ PU	155	15-52	26
MIL-53 (Al)/PDMS/ polyurethane sponge	128.13	12-50.5	27
PU-Cu (BDC)-NGPs	154	43.5-132	28
Dy-MOF@PU	152.62	14-49	29
$Ti_3C_2T_x$/ZIF-8 Functional PU sponge	135	48-91	30
C-F-Ce@PU	153.4	15-45	31
2CF_3-UiO-66@SP	162.03	64-142	This work

Reference

1 H. Park, S. Kim, B. Jung, M. H. Park, Y. Kim, M. Kim, Defect engineering into metal-organic frameworks for the rapid and sequential installation of functionalities, *Inorg. Chem.*, 2018, ***57***, 1040-1047.

2 *Japan Pat.*, Process for the preparation of cobalt complexes, JP2015151350, 2015.

3 P. Horcajada, H. Chevreau, D. Heurtaux, F. Benyettou, F. Salles, T. Devic, A. Garcia-Marquez, C. Yu, H. Lavrard, C. L. Dutson, E. Magnier, G. Maurin, E. Elkaim, C. Serre, Extended and functionalized porous iron(III) tri- or dicarboxylates with MIL-100/101 topologies, *Chem. Commun.*, 2014, ***50***, 6872-4.

4 T. Devic, P. Horcajada, C. Serre, F. Salles, G. Maurin, B. Moulin, D. Heurtaux, G. Clet, A. Vimont, J. M. Grenèche, B. L. Ouay, F. Moreau, E. Magnier, Y. Filinchuk, J. Marrot, J. C. Lavalley, M. Daturi, G. Férey, Functionalization in flexible porous solids: effects on the pore opening and the host-guest interactions, *J. Am. Chem. Soc.*, 2010, ***132***, 1127-1136.

5 C. Adamo, V. Barone, Toward reliable density functional methods without adjustable parameters: The PBE0 model. *J. Chem. Phys.*, 1999, ***110***, 6158-6170.

6 E. Caldeweyher, C. Bannwarth, S. Grimme, Extension of the D3 dispersion coefficient model. *J. Chem. Phys.*, 2017, ***147***, 034112.

7 F. Weigend, R. Ahlrichs, Balanced basis sets of split valence, triple zeta valence and quadruple zeta valence quality for H to Rn: Design and assessment of accuracy. *Phys. Chem. Chem. Phys.*, 2005, ***7***, 3297-3305.

8 A. V. Marenich, C. J. Cramer, D. G. Truhlar, Universal solvation model based on solute electron density and on a continuum model of the solvent defined by the bulk dielectric constant and atomic surface tensions. *J. Phys. Chem. B*, 2009, ***113***, 6378-6396.

9 Y. Zhao, D. G. Truhlar, The M06 suite of density functionals for main group thermochemistry, thermochemical kinetics, noncovalent interactions, excited states, and transition elements: Two new functionals and systematic testing of four M06-class functionals and 12 other functionals. *Theor. Chem. Acc.*, 2008, ***120***, 215-241.

10 W. J. Hehre, R. Ditchfield, J. A. Pople, Self-consistent molecular orbital methods. XII. further extensions of gaussian-typebasis sets for use in molecular orbital studies of organic molecules. *J. Chem. Phys.*, 1972, ***56***, 2257-2261.

11 L. Goerigk, S. Grimme, Efficient and accurate double-hybrid-meta-GGA density functionalss-evaluation with the extended GMTKN30 database for general main group thermochemistry, kinetics, and noncovalent interactions, *J. Chem. Theory Comput.*, 2011, ***7***, 291-309.

12 Y. Che, W. L. Li, W. X. Wu, Z. X. Li, Preparation of fluorine-free robust superhydrophobic fabric via diazonium radical graft polymerization. *Prog. Org. Coat.*, 2023, ***183***, 107721.

13 Y. Yang, W. Huang, Z. Guo, S. Zhang, F. Wu, J. Huang, H. Yang, Y. Zhou, W. Xu, S. Gu, Robust fluorine-free colorful superhydrophobic PDMS/NH_2-MIL-125(Ti)@cotton fabrics

for improved ultraviolet resistance and efficient oil–water separation, *Cellulose*, 2019, ***26***, 9335-9348.

14 R. Dalapati, S. Nandi, C. Gogoi, A. Shome, S. Biswas, Metal-organic framework (MOF) derived recyclable, superhydrophobic composite of cotton fabrics for the facile removal of oil spills, *ACS Appl. Mater. Inter.*, 2021, ***13***, 8563-8573.

15 C. Gogoi, A. Rana, S. Ghosh, R. Fopase, L. M. Pandey, S. Biswas, Superhydrophobic self-cleaning composite of a metal-organic framework with polypropylene fabric for efficient removal of oils from oil-water mixtures and emulsions, *ACS Appl. Nano Mater.*, 2022, ***5***, 10003-10014.

16 G. Zhang, Y. Liu, C. Chen, L. Long, J. He, D. Tian, L. Luo, G. Yang, X. Zhang, Y. Zhang, MOF-based cotton fabrics with switchable superwettability for oil-water separation, *Chem. Eng. Sci.*, 2022, ***256***, 117695.

17 Y. Yang, Z. Guo, W. Huang, S. Zhang, J. Huang, H. Yang, Y. Zhou, W. Xu, S. Gu, Fabrication of multifunctional textiles with durable antibacterial property and efficient oil-water separation via in situ growth of zeolitic imidazolate framework-8 (ZIF-8) on cotton fabric, *Appl. Surf. Sci.*, 2020, ***503***, 144079.

18 D. Li, Z. Guo, Metal-organic framework superhydrophobic coating on Kevlar fabric with efficient drag reduction and wear resistance, *Appl. Surf. Sci.*, 2018, ***443***, 548-557.

19 W. Li, Y. Zhang, Z. Yu, T. Zhu, J. Kang, K. Liu, Z. Li, S. C. Tan, In situ growth of a stable metal-organic framework (MOF) on flexible fabric via a layer-by-layer strategy for versatile applications, *ACS Nano*, 2022, ***16***, 14779-14791.

20 S. Zhang, K. Fang, X. Liu, M. Cheng, D. Liu, X. Qiao, J. Wang, Polymethylhydrosiloxane and ZIF-8/color nanoparticles enhanced the UV-resistance, antibacterial and hydrophobicity performance of cotton fabrics, *Prog. Org. Coat.*, 2023, ***182***, 107702.

21 H. Guan, R. Li, R. Lian, J. Cui, M. Ou, L. Liu, X. Chen, C. Jiao, S. Kuang, A biomimetic design for efficient petrochemical spill disposal: CoFe-PBA modified superhydrophobic melamine sponge with mechanical/chemical durability and low fire risk, *J. Hazard. Mater.*, 2023, ***459***, 132041.

22 J. Piao, M. Lu, J. Ren, Y. Wang, T. Feng, Y. Wang, C. Jiao, X. Chen, S. Kuang, MOF-derived LDH modified flame-retardant polyurethane sponge for high-performance oil-water separation: Interface engineering design based on bioinspiration, *J. Hazard. Mater.*, 2023, ***444***, 130398.

23 J. Xue, L. Zhu, X. Zhu, H. Li, R. Wang, X. Liu, F. Xia, X. Li, Q. Xue, Hierarchical superhydrophobic polydimethylsiloxane/copper terephthalate/polyurethane sponge for highly efficient oil/water separation, *Colloid. Surface. A*, 2021, ***630***, 127635.

24 Y. Zhou, S. Qiu, F. Chu, W. Yang, Y. Qiu, L. Qian, W. Hu, L. Song, High-performance flexible polyurethane foam based on hierarchical BN@MOF-LDH@APTES structure: Enhanced adsorption, mechanical and fire safety properties, *J. Colloid Interface Sci.*, 2022, ***609***, 794-806.

25 D. W. Kim, K. Eum, H. Kim, D. Kim, M. D. d. Mello, K. Park, M. Tsapatsis, Continuous ZIF-8/reduced graphene oxide nanocoating for ultrafast oil/water separation, *Chem. Eng. J.*, 2019, ***372***, 509-515.

26 T. Yu, F. Halouane, D. Mathias, A. Barras, Z. Wang, A. Lv, S. Lu, W. Xu, D. Meziane, N. Tiercelin, S. Szunerits, R. Boukherroub, Preparation of magnetic, superhydrophobic/superoleophilic polyurethane sponge: Separation of oil/water mixture and demulsification, *Chem. Eng. J.*, 2020, ***384***, 123339.

27 I. Riyal, G. Joshi, H. Sharma,C. Dwivedi, Modified hydrophobic and oleophilic polyurethane sponge for oil absorption with MIL-53, *Environ. Res.*, 2023, ***237***, 116982.

28 N. Habibi, S. Faraji, A. Pourjavadi, Nano graphite platelets/Cu (BDC) MOF coating on polyurethane sponge: A superhydrophobic self-extinguishing adsorbent for static and continuous oil/water separation, *Colloid. Surface. A*, 2023, ***676***, 132186.

29 J. Meng, F. Li, T. Li, W. Cao, Coating polyurethane sponge with Dy-MOF for efficient oil-water separation in complex environments, *Appl. Surf. Sci.*, 2023, ***614***, 156183.

30 G. Deng, M. Sun, Y. Shi, Y. Feng, Y. Lv, L. Tang, J. Gao, P. Song, Construction of MXene/MOFs nano-coatings on PU sponge with enhanced interfacial interaction and fire resistance towards efficient removal of liquid hazardous chemicals, *J. Clean. Prod.*, 2023, ***403***, 136887.

31 J. F. Meng, B. Y. Song, F. Li, T. H. Li, Ce-MOF-based superhydrophobic polyurethane sponge reinforced by cellulose for efficient oil-water separation, *Mater. Today Chem.*, 2023, ***28***, 101371.